The Effects of Wave-Dependent Surface Fluxeson CESM2 Climate Simulations

Xiaoming Shi[1], Qing Li[2], Diah Valentina Lestari[3], Shangfei Lin[4], and Hui Su[5]

[1]Division of Environment and Sustainability, Hong Kong University of Science and Technology
[2]The Hong Kong University of Science and Technology (Guangzhou)
[3]School of Civil and Environmental Engineering, Nanyang Technological University, Singapore
[4]Department of Oceanography, Dalhousie University
[5]Hong Kong University of Science and Technology

March 25, 2024

Abstract

Processes at the air-sea interface govern the climate mean state and climate variability by determining the exchange of momentum, heat, and water between the atmosphere and ocean. Traditional climate models compute those exchanges across the air-sea interface by assuming an ocean surface with roughness determined by wind and stability conditions, essentially assuming ocean surface waves are in equilibrium states. In reality, that is rarely the case. Such effects have been emphasized in numerical weather predictions for weather systems like tropical cyclones. An accurate representation of ocean surface waves requires a prognostic ocean surface wave model. The addition of WAVEWATCH III (WW3) to the Community Earth System Model 2 (CESM2) makes it possible to parameterize the impacts of ocean surface waves on momentum and energy exchange. This study documents our implementation of a wave-state-dependent surface flux scheme in CEMS2. Our scheme considers the effects of waves on ocean surface roughness and those of sea spray on surface sensible and latent heat. We found that the new scheme significantly impacts the mean atmospheric circulation and the upper ocean. The errors in mean atmospheric circulation and surface temperature patterns are reduced. The modified surface flux lowers the eddy-driven jet speed and weakens the Hadley circulation. Global mean sea surface temperature (SST) warm bias is reduced due to the cooling of the Southern Ocean and eastern boundary currents. In particular, the eastern Pacific exhibited a weak cooling trend in the historical simulation for the recent decades, reducing the existing SST trend bias in CESM2.

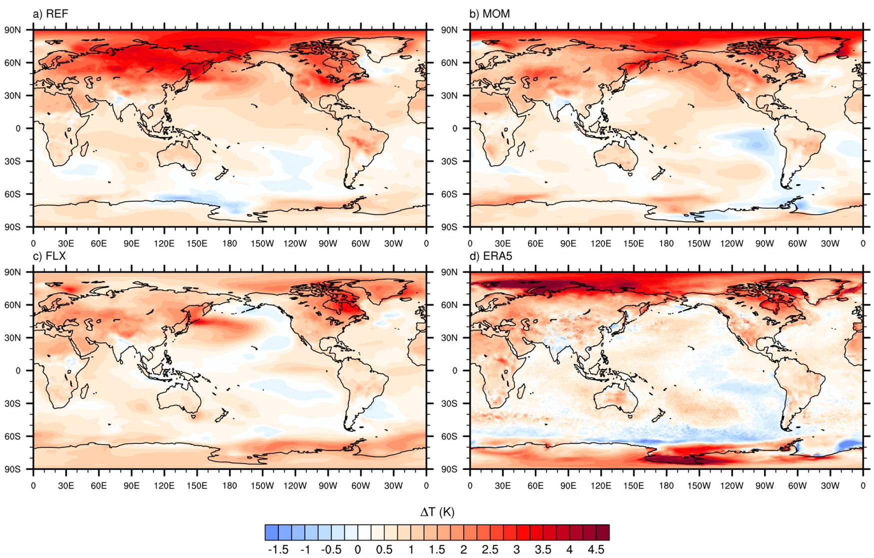
a) REF
b) MOM
c) FLX
d) ERA5
90N
60N
30N
0
30S
60S
90S
0
30E
60E
90E
120E
150E
180
150W
120W
90W
60W
30W
ΔT (K)
-1.5
-1
-0.5
0
0.5
1
1.5
2
2.5
3
3.5
4
4.5

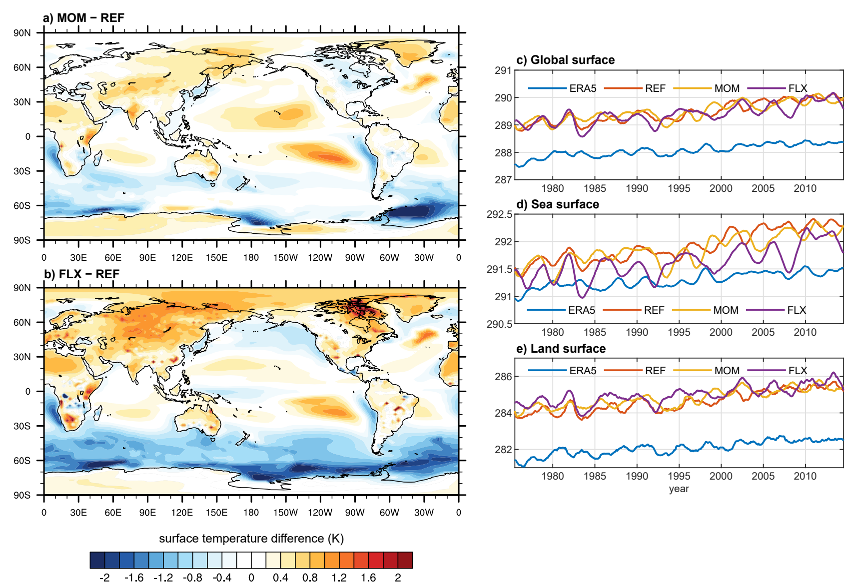
a) MOM − REF
b) FLX − REF
surface temperature difference (K)
-2
-1.6
-1.2
-0.8
-0.4
0
0.4
0.8
1.2
1.6
2
c) Global surface
d) Sea surface
e) Land surface
ERA5
REF
MOM
FLX
year
1980
1985
1990
1995
2000
2005
2010

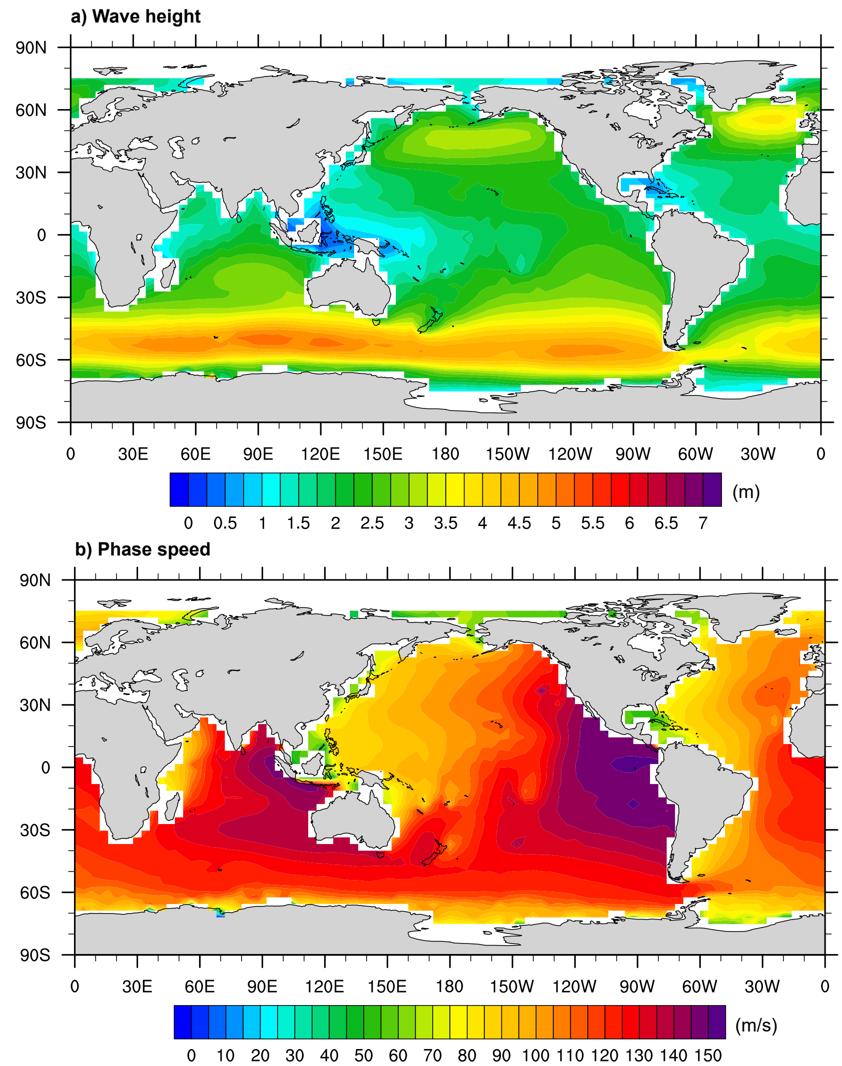
a) Wave height
90N
60N
30N
0
30S
60S
90S
0 30E 60E 90E 120E 150E 180 150W 120W 90W 60W 30W 0
0 0.5 1 1.5 2 2.5 3 3.5 4 4.5 5 5.5 6 6.5 7
(m)
b) Phase speed
90N
60N
30N
0
30S
60S
90S
0 30E 60E 90E 120E 150E 180 150W 120W 90W 60W 30W 0
0 10 20 30 40 50 60 70 80 90 100 110 120 130 140 150
(m/s)

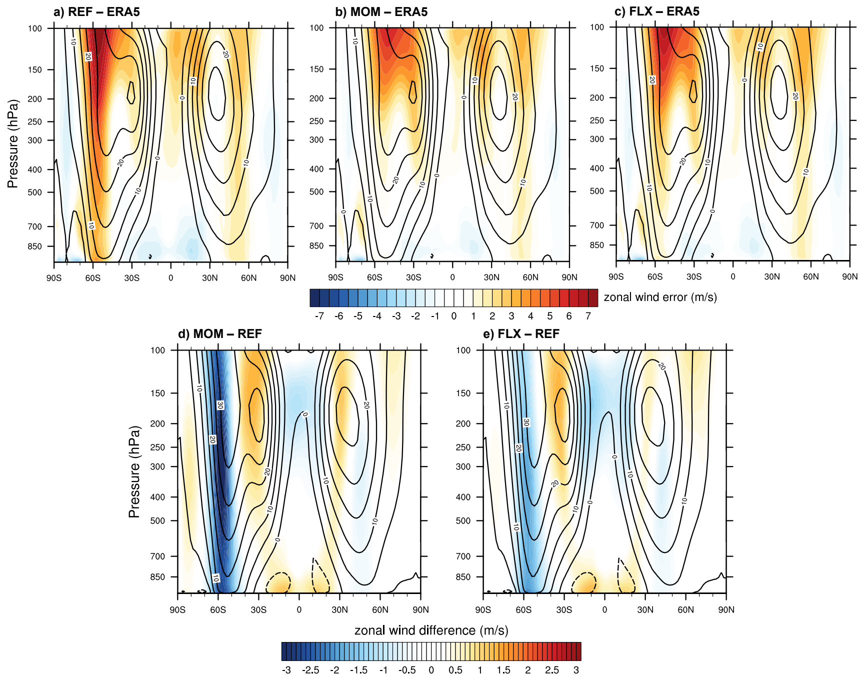

a) REF – ERA5
b) MOM – ERA5
c) FLX – ERA5
Pressure (hPa)
zonal wind error (m/s)
d) MOM – REF
e) FLX – REF
zonal wind difference (m/s)

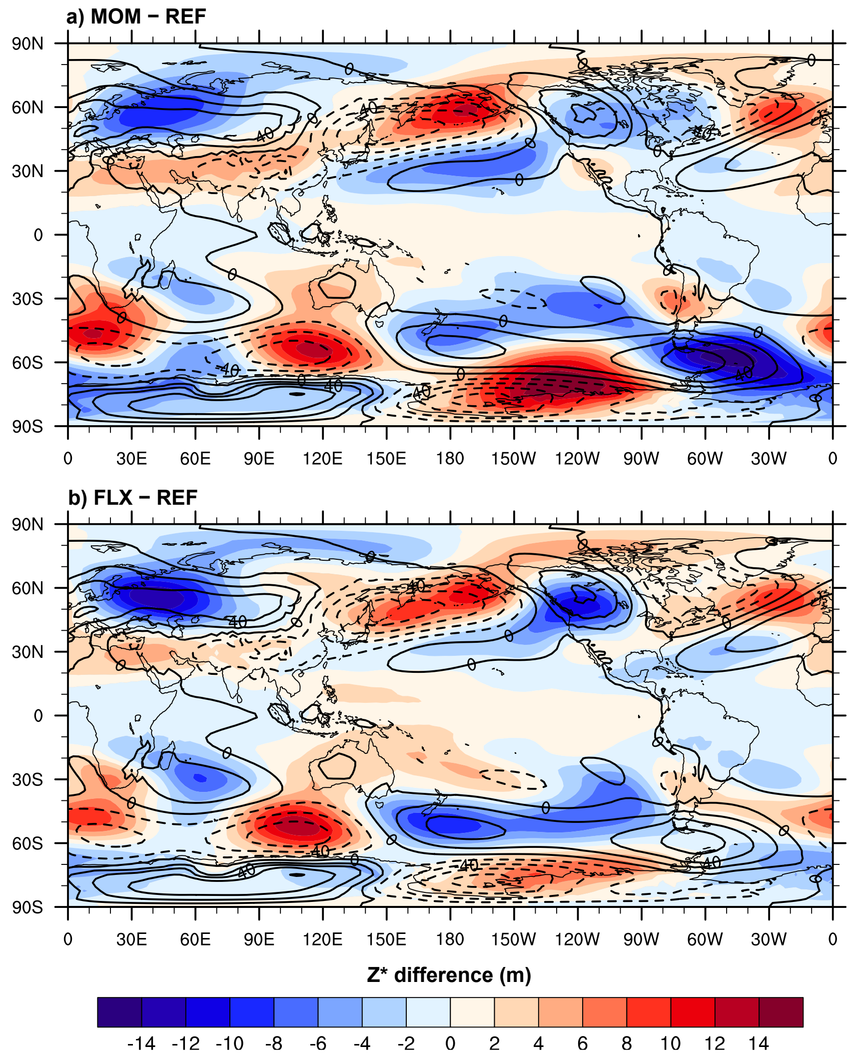

a) MOM − REF
b) FLX − REF
90N
60N
30N
0
30S
60S
90S
0
30E
60E
90E
120E
150E
180
150W
120W
90W
60W
30W
Z* difference (m)
-14 -12 -10 -8 -6 -4 -2 0 2 4 6 8 10 12 14

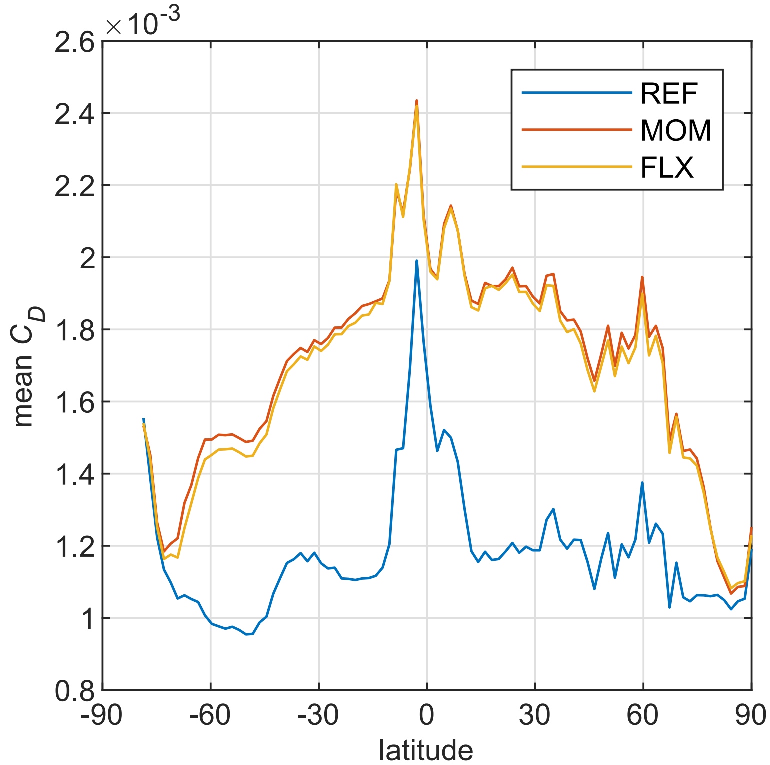
×10^-3
2.6
2.4
2.2
2
1.8
1.6
1.4
1.2
1
0.8
mean C_D
-90
-60
-30
0
30
60
90
latitude
REF
MOM
FLX

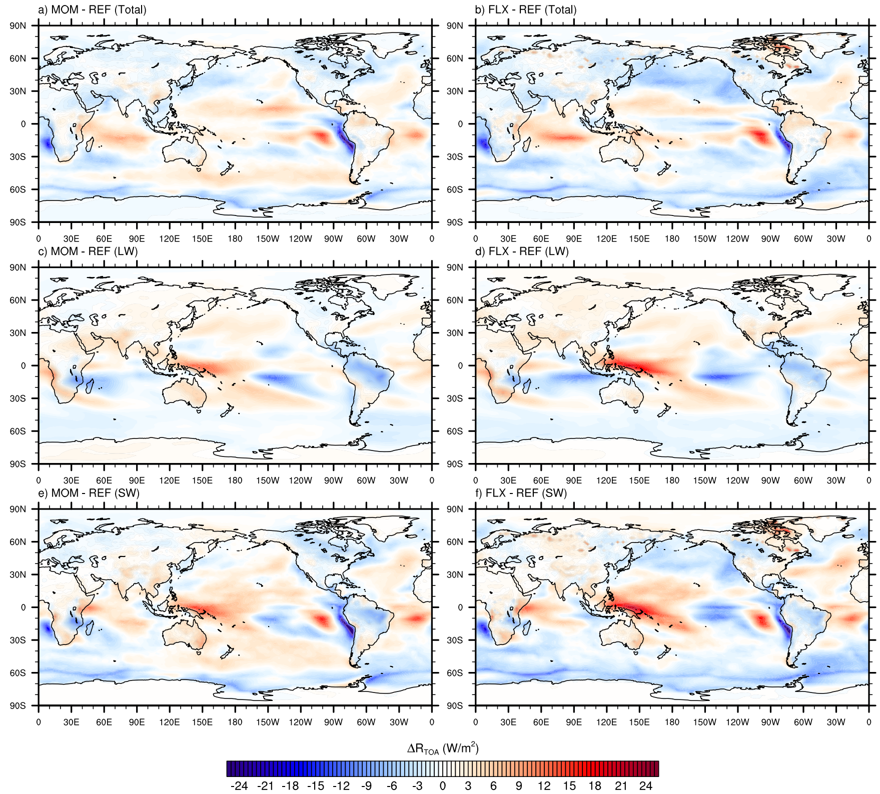

a) MOM - REF (Total)
b) FLX - REF (Total)
c) MOM - REF (LW)
d) FLX - REF (LW)
e) MOM - REF (SW)
f) FLX - REF (SW)
90N
60N
30N
0
30S
60S
90S
0
30E
60E
90E
120E
150E
180
150W
120W
90W
60W
30W
ΔR_TOA (W/m²)
-24 -21 -18 -15 -12 -9 -6 -3 0 3 6 9 12 15 18 21 24

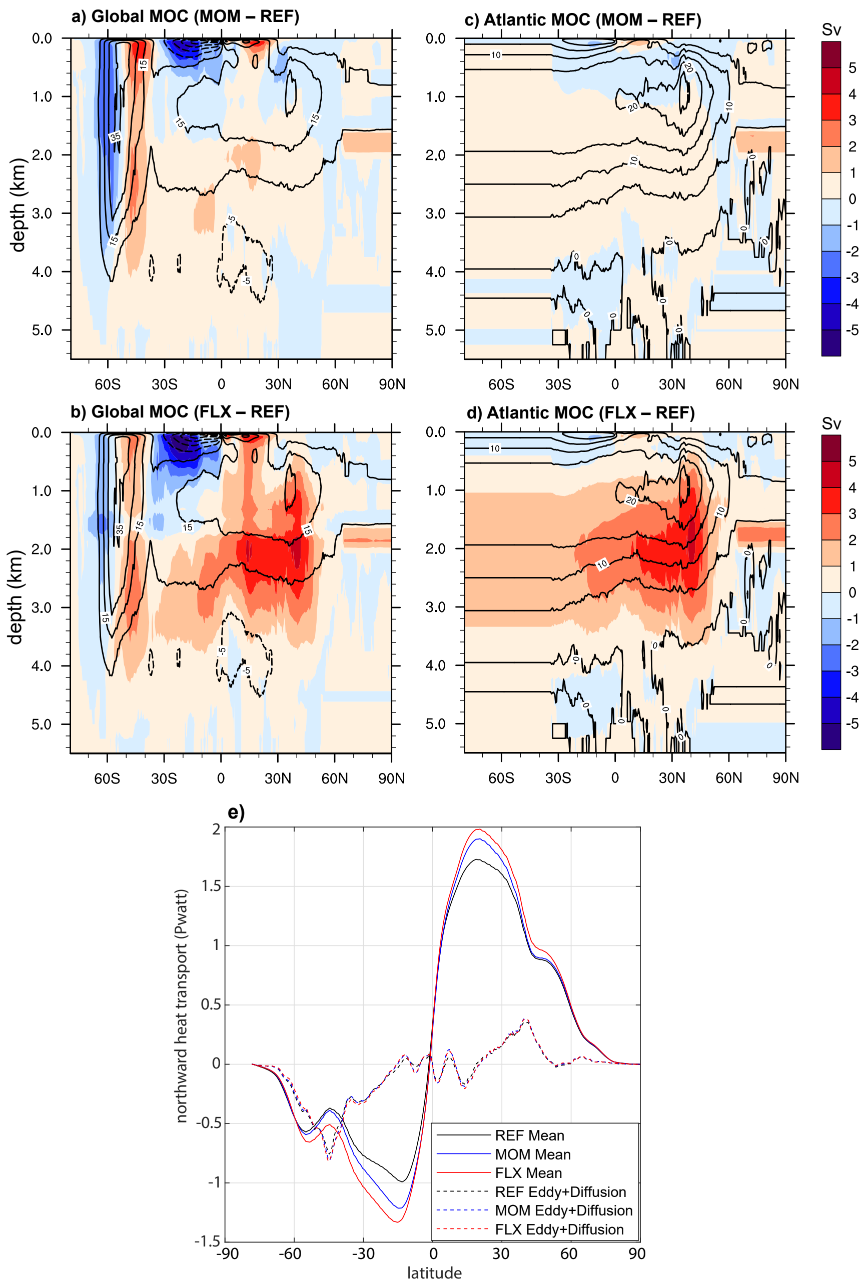
a) Global MOC (MOM – REF)
b) Global MOC (FLX – REF)
c) Atlantic MOC (MOM – REF)
d) Atlantic MOC (FLX – REF)
depth (km)
Sv
60S
30S
0
30N
60N
90N
e)
northward heat transport (Pwatt)
latitude
REF Mean
MOM Mean
FLX Mean
REF Eddy+Diffusion
MOM Eddy+Diffusion
FLX Eddy+Diffusion

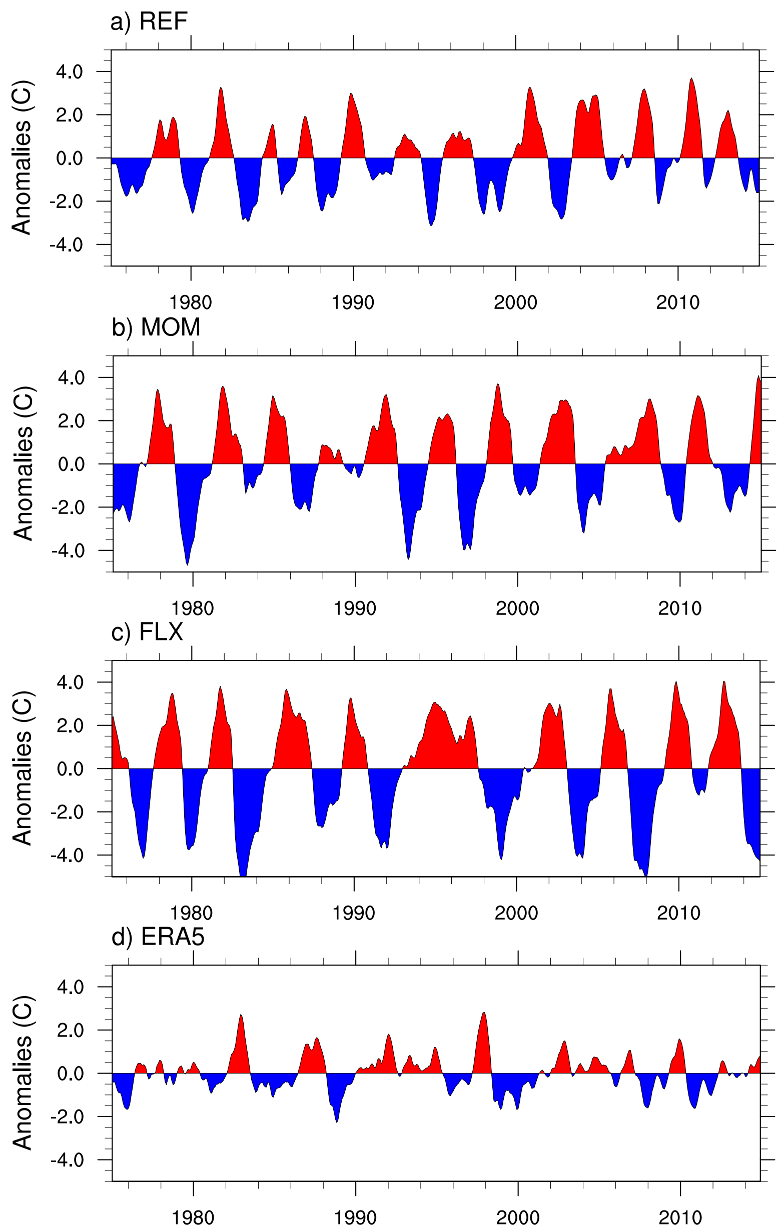

a) REF
b) MOM
c) FLX
d) ERA5
Anomalies (C)
4.0
2.0
0.0
-2.0
-4.0
1980
1990
2000
2010

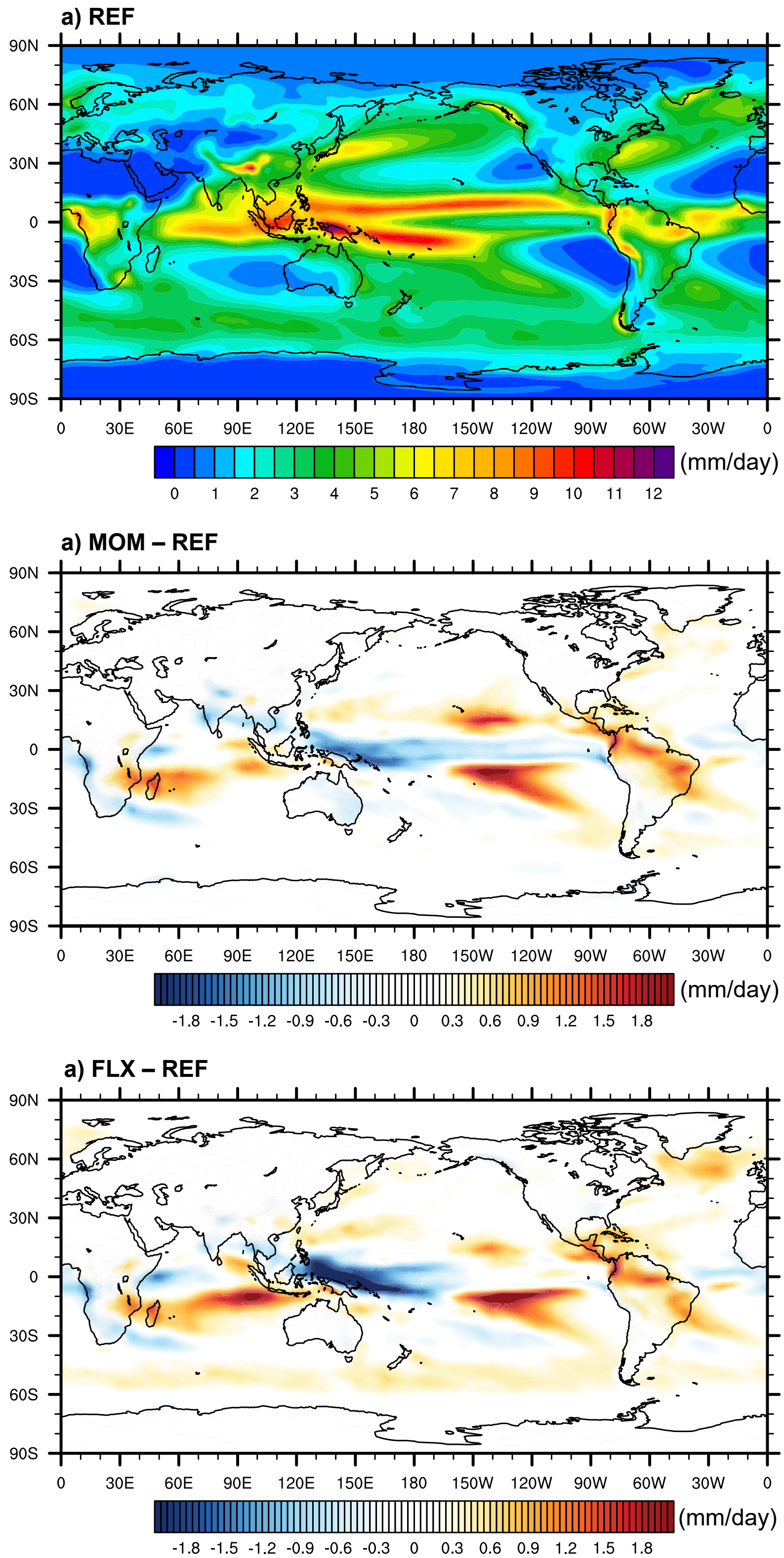
a) REF
90N
60N
30N
0
30S
60S
90S
0
30E
60E
90E
120E
150E
180
150W
120W
90W
60W
30W
0
(mm/day)
0 1 2 3 4 5 6 7 8 9 10 11 12
a) MOM – REF
(mm/day)
-1.8 -1.5 -1.2 -0.9 -0.6 -0.3 0 0.3 0.6 0.9 1.2 1.5 1.8
a) FLX – REF
(mm/day)
-1.8 -1.5 -1.2 -0.9 -0.6 -0.3 0 0.3 0.6 0.9 1.2 1.5 1.8

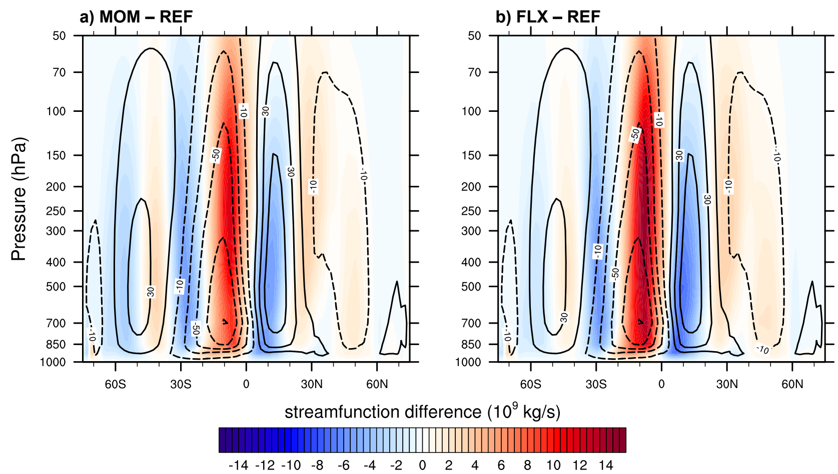
a) MOM – REF
b) FLX – REF
Pressure (hPa)
60S 30S 0 30N 60N
streamfunction difference (10^9 kg/s)
-14 -12 -10 -8 -6 -4 -2 0 2 4 6 8 10 12 14

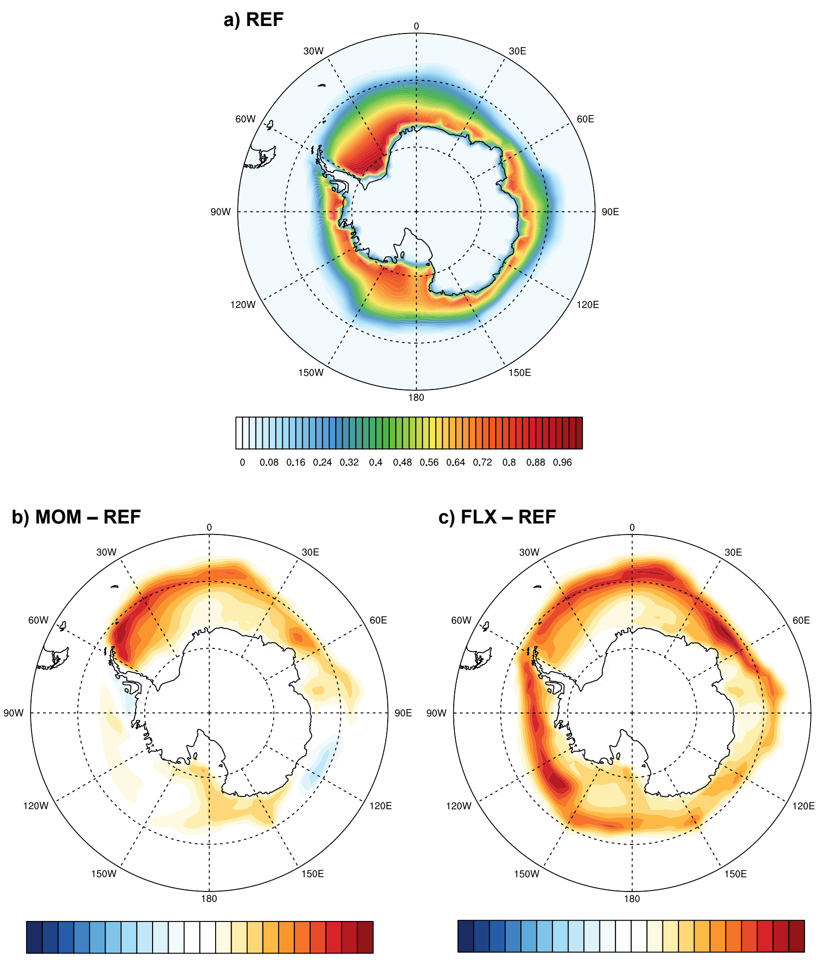
a) REF
0 0.08 0.16 0.24 0.32 0.4 0.48 0.56 0.64 0.72 0.8 0.88 0.96
b) MOM – REF
c) FLX – REF
-0.2 -0.16 -0.12 -0.08 -0.04 0 0.04 0.08 0.12 0.16 0.2

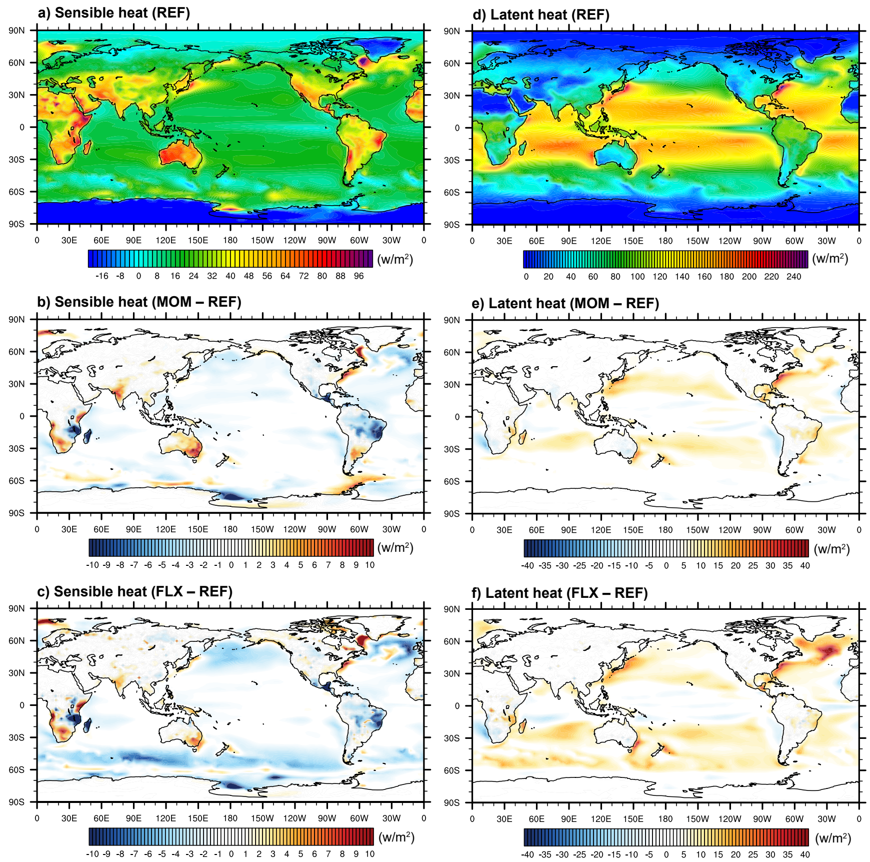
a) Sensible heat (REF)
d) Latent heat (REF)
b) Sensible heat (MOM – REF)
e) Latent heat (MOM – REF)
c) Sensible heat (FLX – REF)
f) Latent heat (FLX – REF)
90N 60N 30N 0 30S 60S 90S
0 30E 60E 90E 120E 150E 180 150W 120W 90W 60W 30W 0
-16 -8 0 8 16 24 32 40 48 56 64 72 80 88 96
0 20 40 60 80 100 120 140 160 180 200 220 240
-10 -9 -8 -7 -6 -5 -4 -3 -2 -1 0 1 2 3 4 5 6 7 8 9 10
-40 -35 -30 -25 -20 -15 -10 -5 0 5 10 15 20 25 30 35 40
(w/m2)

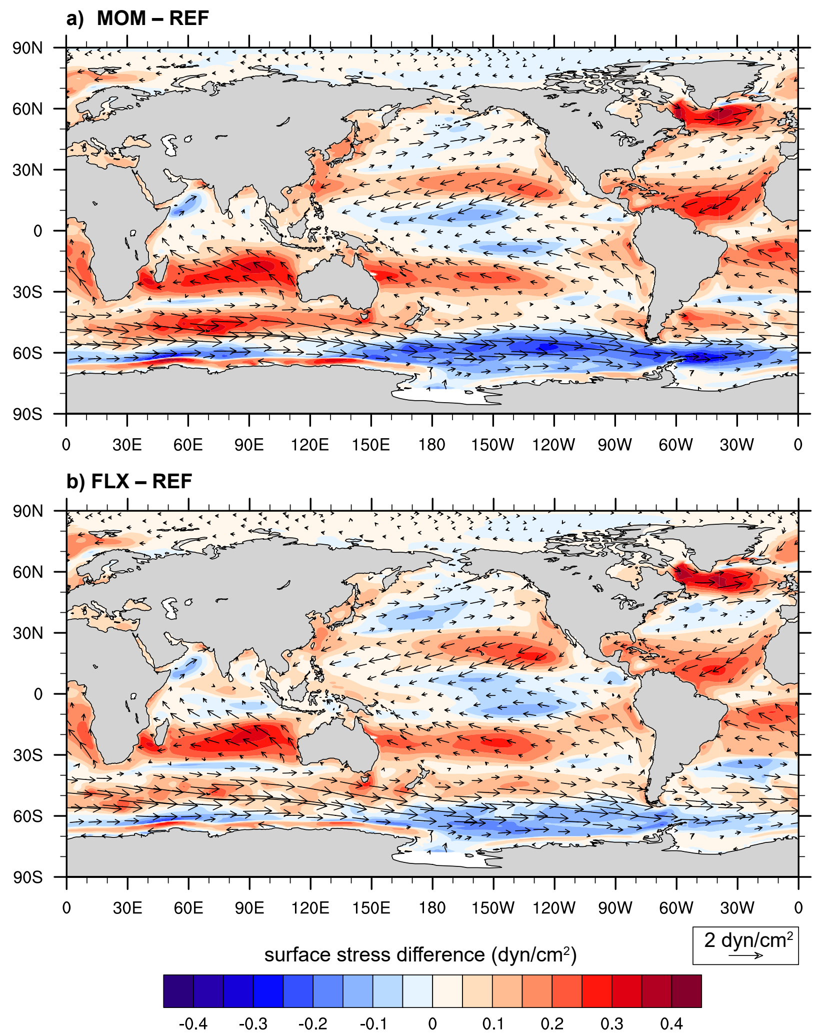

a) MOM – REF
b) FLX – REF
90N
60N
30N
0
30S
60S
90S
0
30E
60E
90E
120E
150E
180
150W
120W
90W
60W
30W
2 dyn/cm²
surface stress difference (dyn/cm²)
-0.4
-0.3
-0.2
-0.1
0.1
0.2
0.3
0.4

The Effects of Wave-Dependent Surface Fluxes on CESM2 Climate Simulations

Xiaoming Shi[1,2], Qing Li[2,3], Diah Valentina Lestari[4], Shangfei Lin[2,5], Hui Su[6]

[1]Division of Environment and Sustainability, Hong Kong University of Science and Technology, Hong Kong, China

[2]Center for Ocean Research in Hong Kong and Macau, Hong Kong University of Science and Technology, Hong Kong, China

[3]Earth, Ocean and Atmospheric Sciences Thrust, Hong Kong University of Science and Technology (Guangzhou), Guangzhou, China

[4]School of Civil and Environmental Engineering, Nanyang Technological University, Singapore

[5]Department of Mathematics, Hong Kong University of Science and Technology, Hong Kong, China

[6]Department of Civil and Environmental Engineering, Hong Kong University of Science and Technology, Hong Kong, China

Key Points:

- A wave-state dependent surface flux parameterization is implemented in the Community Earth System Model version 2 (CESM2).
- The new scheme reduces biases in the mean climate state, such as barotropic jet in the Southern Hemisphere and sea surface temperature.
- The scheme also reproduces the weak cooling in the eastern Pacific observed in recent decades, missing in CESM2 and other climate models.

Corresponding author: Xiaoming Shi, `shixm@ust.hk`

Abstract

Processes at the air-sea interface govern the climate mean state and climate variability by determining the exchange of momentum, heat, and water between the atmosphere and ocean. Traditional climate models compute those exchanges across the air-sea interface by assuming an ocean surface with roughness determined by wind and stability conditions, essentially assuming ocean surface waves are in equilibrium states. In reality, that is rarely the case. Such effects have been emphasized in numerical weather predictions for weather systems like tropical cyclones. An accurate representation of ocean surface waves requires a prognostic ocean surface wave model. The addition of WAVEWATCH III (WW3) to the Community Earth System Model 2 (CESM2) makes it possible to parameterize the impacts of ocean surface waves on momentum and energy exchange. This study documents our implementation of a wave-state-dependent surface flux scheme in CEMS2. Our scheme considers the effects of waves on ocean surface roughness and those of sea spray on surface sensible and latent heat. We found that the new scheme significantly impacts the mean atmospheric circulation and the upper ocean. The errors in mean atmospheric circulation and surface temperature patterns are reduced. The modified surface flux lowers the eddy-driven jet speed and weakens the Hadley circulation. Global mean sea surface temperature (SST) warm bias is reduced due to the cooling of the Southern Ocean and eastern boundary currents. In particular, the eastern Pacific exhibited a weak cooling trend in the historical simulation for the recent decades, reducing the existing SST trend bias in CESM2.

Plain Language Summary

The ocean and the atmosphere are both essential components of the Earth system. They exchange momentum, heat, and water at the air-sea interface. Traditionally, those exchanges are estimated based on atmospheric stability, wind, and air-sea differences in temperature and humidity, which are assumed to determine microscale turbulence. Ocean surface waves can potentially change the morphology of the air-sea interface and, therefore, affect turbulence. Sea spray generated in waves can also enhance water vapor transport into the atmosphere via the evaporation of small droplets. However, those enhancements depend on wave states such as wave height and phase speed, which were traditionally not simulated in Earth system models. The WAVEWATCH III (WW3) model has recently been added to the Community Earth System Model 2 (CESM2) to compute wave states and improve ocean surface mixing. In this work, we developed a new scheme in CESM2 to include the effects of ocean surface waves on air-sea momentum, heat, and water exchanges. We found that the new methods reduce lower-level wind speed in the atmosphere and introduce meaningful improvements in temperature, precipitation, and ocean circulation. The improved wave-state-dependent air-sea coupling in CESM2 can yield more realistic climate simulations regarding the mean states and historical trends.

1 Introduction

The ocean and atmosphere coupling is critical in the Earth system. It determines the development of short-term weather phenomena and modulates low-frequency climate variabilities. For instance, tropical cyclones (TCs) draw energy from the ocean through sea surface enthalpy flux (Emanuel, 1986), and previous studies from world-leading numerical weather prediction (NWP) agencies have demonstrated that atmosphere-ocean coupling plays an essential role in TC intensity prediction (Mogensen et al., 2017; Wada et al., 2018; Yu et al., 2013; Bernardet et al., 2015). TC intensity errors in the ECMWF Reanalysis version 5 (ERA5) have also been found to correlate with its bias in surface enthalpy flux (Zhao et al., 2022). For climate projections, lacking atmosphere-ocean coupling can limit a climate model's skills in simulating natural climate variability (Barsugli & Battisti, 1998; He & Soden, 2016). Such influences are especially notable for El Niño-Southern Oscillation (ENSO), Asia monsoon, and temperature and precipitation extremes (Newman et al., 2009; Zhu & Shukla, 2013; Hirons et al., 2018; Fischer et al., 2018).

The exchange of momentum, enthalpy, aerosols, and CO_2 governs the influence of atmosphere-ocean coupling. What complicates this coupling is the existence of ocean surface gravity waves, which can modify ocean surface roughness, generate sea spray, and induce Langmuir mixing in the ocean surface boundary layer, among other effects (Cavaleri et al., 2012). Comparison of simulations with direct measurements from the Coupled Boundary Layer Air-Sea Transfer (CBLAST) field experiment suggests that reanalysis products substantially underestimate latent heat flux under TC conditions, and including surface wave-related effects can reduce such bias (Liu et al., 2011). Meanwhile, including ocean-atmosphere-wave coupling has been found effective in improving wind and wave simulation accuracy (Olabarrieta et al., 2012). A few regional ocean-atmosphere-wave coupled models have been developed and evaluated in TC simulations, and the dependency on wave state helps those models improve the simulated TC intensity and structure (Warner et al., 2010; S. S. Chen et al., 2013; Pianezze et al., 2018; Zhao et al., 2022).

However, the effects of ocean waves on air-sea interaction in Earth system models are only considered in limited studies. Song et al. (2012) coupled the marine science and numerical modeling (MASNUM) surface wave model with the ocean component of the Community Climate System Model Version 3 (CCSM3) to represent nonbreaking wave-induced vertical mixing, and they found tropical SST was much improved. Qiao et al. (2013) coupled the MASNUM wave model with other components in the First Institute of Oceanography-Earth System Model (FIO-ESM), which was the first to include surface waves among all the climate models participating in the Coupled Model Intercomparison Project Phase 5 (CMIP5). Using a coupled atmosphere-wave model, Shimura et al. (2017) evaluated how wave-dependent estimation of sea surface roughness may influence the mean climate state in their simulations and found tropical winds are enhanced, which leads to significant changes in the Hadley circulation. Bao et al. (2020) developed FIO-ESM v2.0, which included the effect of surface wave Stokes drifts on air-sea momentum and heat fluxes and wave-induced sea spray on air-sea heat fluxes. In particular, FIO-ESM v2.0 reduced the significant warm bias of sea surface temperature near the eastern boundary of the tropical Pacific in FIO-ESM v1.0, a common challenge for all climate models (Bao et al., 2020). Lee et al. (2021) assessed all 59 CMIP6 climate models regarding their skills in reconstructing historical ENSO events, and they found FIO-ESM v2.0 had the best performance.

The recent implementation of WAVEWATCH III (WW3) into the Community Earth System Model (CESM) by Li et al. (2016) provides an excellent opportunity for studying the impact of active ocean-wave-atmosphere coupling on the climate simulation in an Earth system model. Li et al. (2016) demonstrated that biases of ocean mixed layer depth, temperature, and ocean ventilation are effectively reduced by parameterizing the Langmuir mixing based on wave state. Active atmosphere-wave coupling, or more precisely, surface flux-wave coupling, was not included in CESM yet. Conventional approaches relate surface fluxes of momentum, heat, and moisture to the air-sea gradient of wind, temperature, and moisture mixing ratio. Introducing wave-state dependence allows a more accurate calculation of the fluxes and, therefore, a better representation of the air-sea interaction in the presence of waves.

In this study, we implement a wave-dependent sea surface roughness length parameterization and add sea spray-induced fluxes into CESM2. We describe the details of the parameterization and its implementation in Section 2. In Section 3 and 4, we describe the impact of the new parameterization on the simulated surface fluxes and climate states. We summarize our main findings in Section 5, together with a brief discussion on the limitations and implications of this study, an effort towards a full ocean-atmosphere-wave coupling in Earth system modeling.

2 Methods and Experiments

2.1 Wave-Dependent Fluxes

The original CESM2 bulk formulas for turbulence fluxes of momentum (τ), water (E), and sensible heat (H) are the following (Neale et al., 2010),

$$\tau = \rho_A |\Delta \mathbf{V}| C_D \Delta \mathbf{V} \tag{1}$$

$$E = \rho_A |\Delta \mathbf{V}| C_E \Delta q \tag{2}$$

$$H = \rho_A |\Delta \mathbf{V}| C_p C_H \Delta \theta \tag{3}$$

where ρ_A is surface air density, C_p is the specific heat of air at constant pressure, $\Delta \mathbf{V} = \mathbf{V}_A - \mathbf{V}_s$ is the velocity difference between the wind of the lowest atmospheric model level and ocean surface current, $\Delta\theta = \theta_A - T_s$ is the difference between the potential temperature at the lowest atmospheric model level and sea surface temperature, and $\Delta q = q_A - q_s(T_s)$ is the difference between the specific humidity at the lowest model level and the surface saturation specific humidity at the sea surface temperature. The transfer coefficients, C_D, C_E, and C_H, are functions of stability ζ and the momentum roughness length Z_0, which themselves depend on surface fluxes. The system of equations is solved by iteration.

2.1.1 Wave-Dependent Roughness

Our first modification of the surface exchange formulations is updating the momentum roughness. In the original CESM2,

$$Z_0 = 10 \exp\left[-\kappa \left(\frac{c_4}{U_{10}} + c_5 + c_6 U_{10}\right)^{-1}\right] \tag{4}$$

where c_4, c_5, and c_6 are fitting coefficients, κ is von Kàrman constant, and U_{10} is the 10-m wind speed which depends on stability and the neutral condition 10-m drag coefficient $C_{10}^N = c_4 U_{10}^{-1} + c_5 + c_6 U_{10}$.

Our new formulation follows Lin et al. (2021). The sea surface roughness is decomposed to a smooth flow component Z_0^s due to viscosity and rough flow component Z_0^r that is driven by surface gravity waves,

$$Z_0 = Z_0^s + Z_0^r \tag{5}$$

The smooth flow component is given as (Fairall et al., 2003)

$$Z_0^s = 0.11\nu/u_* \tag{6}$$

where ν is the kinematic viscosity of the air and u_* is the air side friction velocity. The rough flow component is given by Lin et al. (2021) is

$$Z_0^r = \begin{cases} 4.54 h_s (c_p/u_*)^{-3.90}, & c_p/u_* < 12 \\ 5.61 \times 10^{-3} h_s (c_p/u_*)^{-1.20}, & 12 \le c_p/u_* < 30 \\ 1.57 \times 10^{-5} h_s (c_p/u_*)^{0.50}, & c_p/u_* \ge 30 \end{cases} \tag{7}$$

which is a function of significant wave heights h_s and wave age, c_p/u_*, with c_p being the peak phase speed of waves.

In this parameterization, the roughness length has different relations with the wave age under wind-sea-dominated, mixed, and swell-dominated sea states. This setting is configured according to Lin and Sheng (2020), who found that the drag coefficient decreases with increasing wave age under wind-sea-dominated and mixed sea states while increases with increasing wave age in swell-dominated sea states. The drag coefficient predicted by the new parameterization is enhanced at low winds and levels off at high winds as compared with equation (4). To implement this new parameterization of surface roughness length for surface fluxes in CESM2, we modified the code of the coupler in CESM2 to receive the significant wave height H_s and peak wave phase speed c_p from WW3. In the coupler, the original equation (4) is replaced by equations (5) to (7) when computing surface fluxes.

2.1.2 Sea Spray-Induced Fluxes

Sea spray droplets are generated due to wave breaking. In most situations, the evaporation of those droplets enhances latent flux and reduces sensible heat to the atmosphere. Based on cloud microphysics, a bulk microphysical model was developed to calculate the sea spray-induced sensible and latent heat fluxes (Andreas, 1989, 1990, 1992, 1995, 1998). However, this bulk model considers a spectrum of droplets with varying sizes and is complex and computationally inefficient.

Andreas et al. (2008) observed that the sea spray-induced latent and sensible flux has a large magnitude for droplets with radii around 50 μm and 100 μm, respectively. Therefore, they hypothesized that the microphysical behavior of droplets at those radii might be good indicators of sea spray-induced fluxes. With this hypothesis, Andreas et al. (2015) developed a fast spray-flux algorithm, in which

$$E_{sp} = \rho_w \left\{ 1 - \left[\frac{r(\tau_{f,50})}{50\mu\text{m}} \right]^3 \right\} V_E(u_*) \tag{8}$$

$$H_{sp} = \rho_w C_w (T_s - T_{eq,100}) V_S(u_*) \tag{9}$$

Here, ρ_w is seawater density, C_w is the specific heat of water, $\tau_{f,50}$ is the residence time of droplets with 50 μm initial radius, $r(\tau_{f,50})$ is the radius of those droplets when they fall back into the sea, and $T_{eq,100}$ is the equilibrium temperature of droplets with 100 μm initial radius. V_E and V_S are wind function (with the unit of $\text{m}\,\text{s}^{-1}$)that depends on the friction velocity u_*,

$$V_E = \begin{cases} 1.76 \times 10^{-9}, & 0 \le u_* \le 0.1358 \\ 2.08 \times 10^{-7} u_*^{2.39}, & u_* > 0.1358 \end{cases} \tag{10}$$

$$V_S = \begin{cases} 3.92 \times 10^{-8}, & 0 \le u_* \le 0.1480 \\ 5.02 \times 10^{-6} u_*^{2.54}, & u_* > 0.1480 \end{cases} \tag{11}$$

$\tau_{f,50}$ and $T_{eq,100}$ depend on wave height from WW3. Further details about their calculation are provided in Andreas et al. (2015) and references therein.

To incorporate the effects of sea spray-induced fluxes in CESM2, we modify the moisture and sensible heat fluxes in equations (2) and (3) according to

$$E_T = E - E_{sp} \tag{12}$$

$$H_T = H - H_{sp} \tag{13}$$

where E_T and H_T are total moisture and sensible heat fluxes, respectively. Note that negative signs are applied to E_{sp} and H_{sp} in the above equations because CESM2 coupler's original fluxes according to equations (2) and (3) are defined with downward flux (atmosphere to ocean) being the positive directions.

2.2 Climate Simulations

We implemented the new algorithms above into CESM2 version 2.2.0. Three historical simulations are conducted to evaluate the impact of the new wave-dependent fluxes on the CESM2 simulation,

1) **REF**: using the original CESM2 code without any changes;
2) **MOM**: including the formulation of wave-dependent roughness length calculation, but not the sea spray effects;
3) **FLX**: including both the new roughness length and sea spray-induced fluxes in its code.

These three parallel experiments differentiate the effects of the new roughness and sea spray flux computation.

We conducted fully coupled CESM2 simulations under transient historical forcing (compset BHIST). The simulation runs from 1850 to 2014. We run the REF simulation for the entire period. The MOM and FLX simulations were branch runs from the REF simulation after 100 years of simulation, running from 1951 to 2014. Throughout this study, if not specified otherwise, we used the last 40 years (1975-2014) of the simulation data for analysis. This allows the three simulations to diverge and is sufficient to illustrate the differences among the three simulations.

The atmosphere and land components run on a latitude-longitude grid of 1.9° by 2.5°. The ocean and sea ice components run on a nominal 1° grid with displaced North Pole at Greenland. The ocean surface wave component runs on a near-global latitude-longitude grid of 3.2° by 4.0°, with polar caps at 78°N/S. We acknowledge that the resolution for WW3 is relatively low, which might cause biases in the representation of wave states. But this is the standard resolution used in CESM2 in its contribution to CMIP6 and is sufficient for our purposes to demonstrate the influence of wave states on the air-sea fluxes on a global scale.

3 Surface Fluxes

Here, we first examine the changes in surface fluxes due to the introduction of wave state dependency. Figure 1 shows the 40-year averaged ocean surface wind stress in the REF simulation with vectors and the change in the magnitude of wind stress relative to REF with color shading. Mid-latitude westerlies and tropical easterlies determine the REF simulation's wind stress pattern. The wind stress on the eastern boundary currents, such as the flow near the western coast of the Americas, has a notable meridional component.

Comparing the MOM and REF simulations, the dominant change in mid- and high-latitudes is the weakening of the westerly wind stress near the Antarctica coast, especially in the Southern Ocean off the West Antarctica coast. Meanwhile, the westerly wind stress in the Southern Ocean around the East Antarctica exhibits some strengthening. Subtropical latitudes exhibit enhancement of wind stresses, especially in regions with a significant meridional component, such as the subtropical Atlantic Ocean and the Southern Hemisphere Indian Ocean. However, the equatorial Pacific Ocean exhibits weakening of easterly wind stress. The FLX simulation exhibits similar patterns to MOM, but the reduced westerly wind stress in the Southern Ocean off West Antarctica and enhanced westerly stress in the Southern Ocean off East Antarctica are suppressed.

However, the actual change in wind stress can be caused by changes in near-surface wind conditions, the drag coefficient C_D, or both. Figure 2 shows the time mean and zonal mean of the drag coefficient. At most latitudes, the wave-dependent roughness length caused about 50% increases in the drag coefficient over the ocean surface. Thus, it is clear that if there were no change in wind conditions, we should see an enhancement of wind stress everywhere over the ocean. The weakening in the Southern Ocean, North and Equatorial Pacific, and North Atlantic Ocean is due to weakened near-surface wind conditions. The drag coefficient in the FLX simulation is slightly smaller than that in the MOM simulation, especially in the Southern Ocean, suggesting that the FLX simulation's near-surface condition is marginally more stable. This is probably related to the additional cooling of SST in FLX compared with MOM, which is described in the next section.

Some characteristics of the wind stress change can be explained directly by the characteristics of wave states. Figure 3 shows the time mean distribution of significant wave height and peak wave speed. The most energetic wave conditions occur in the Southern Ocean as a result of the extended fetch provided for the high westerly winds. Similar high significant wave heights exist in the North Pacific and North Atlantic Oceans. Peak wave speeds are high in the eastern tropical Pacific, Atlantic, and Indian Ocean, consistent with the observed distribution of swell pools (e.g., G. Chen et al., 2002; Semedo et al., 2011). The high waves in the Southern Ocean and North Pacific probably generated intense drag to the atmosphere, lowering the climatological mean wind conditions in those regions. In swell-dominated (high wave age) conditions, sea surface roughness increases with wave phase speed [equation (7)]. Thus, the enhancement of easterly wind stress in tropical oceans, especially the change in eastern boundary currents, should be partially due to the high wave age in the swell

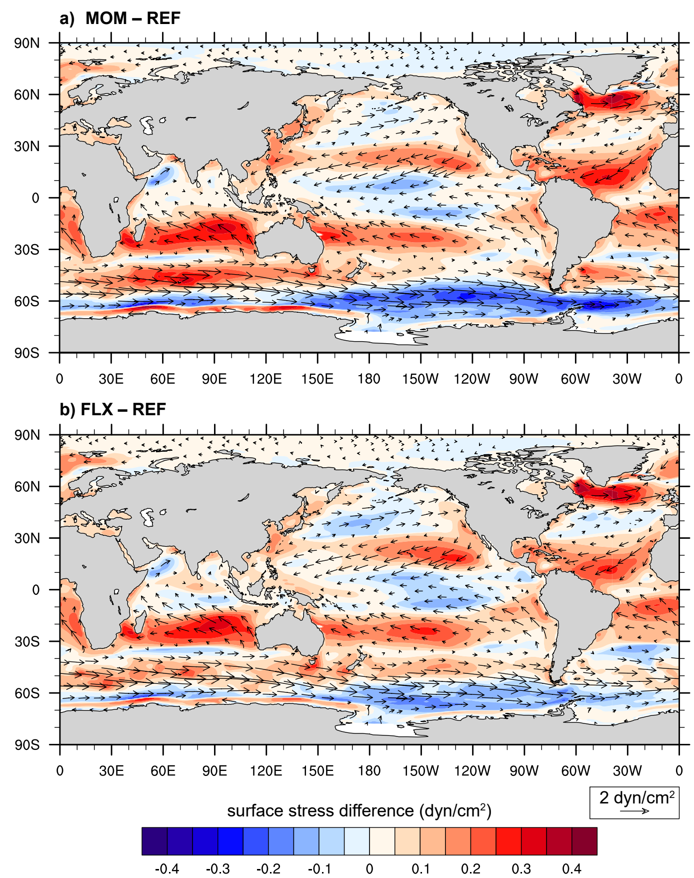

Figure 1. Ocean surface wind stress in the REF simulation (vectors) and the difference in stress magnitude (color shading) between a) MOM and REF, and b) FLX and REF simulations. Note that the stress is the momentum flux into the ocean. Data for 1975-2014 are averaged in time for the analysis.

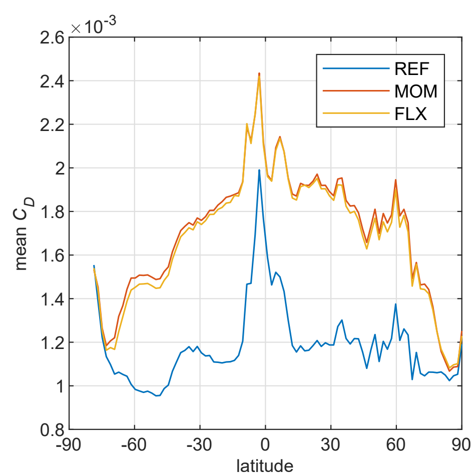

Figure 2. Time mean, zonal mean of the momentum transfer coefficient C_D over ocean surface in simulations.

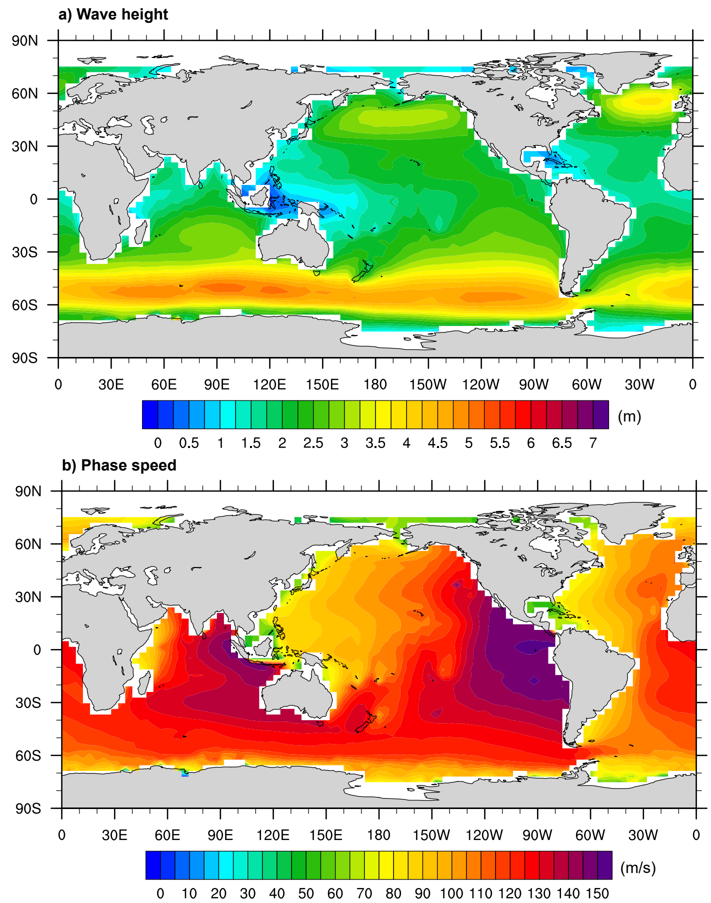

Figure 3. Significant wave height h_s (a) and peak wave speed C_p (b) in the FLX simulation. Data for 1975–2014 are averaged in time for the analysis.

pools. Overall, changes in the wind stress are jointly governed by the wave-dependent roughness and nonlinear response of atmospheric circulation. The former changes the sea surface drag and varies spatially in accordance with wave characteristics. The latter directly modifies the wind speed.

Figure 4 shows the climatological mean surface sensible and latent heat fluxes into the atmosphere in the REF simulation and the changes in MOM and FLX due to introducing the wave-dependent roughness and sea spray-induced fluxes. The MOM simulation has slight decreases in sensible heat flux over most ocean surface areas (Fig. 4b). The drag coefficients for heat fluxes (C_H and C_E) depend not only on the roughness length of latent and sensible heat but also on the roughness length of momentum. It appears that sensible heat flux increased only in the Gulf Stream region. The decrease in sensible heat over the ocean surface is found to be a result of decreases in the near-surface wind (see the next section), which is ubiquitous due to the enhanced momentum drag (Fig. 2). However, the change in latent heat flux (Fig. 4e) is larger than the magnitude of sensible heat flux, and we found that the increases in those subtropical ocean surface are related to sea surface temperature increases in those regions (see next section). Notably, the latent heat flux in the Gulf Stream and Kuroshio current significantly increases, possibly caused by the increase in momentum roughness length and friction velocity.

The FLX simulation exhibits more decreases in sensible heat flux in the Southern Ocean and North Pacific Ocean than MOM, and we will show in the next section that this is also related to the

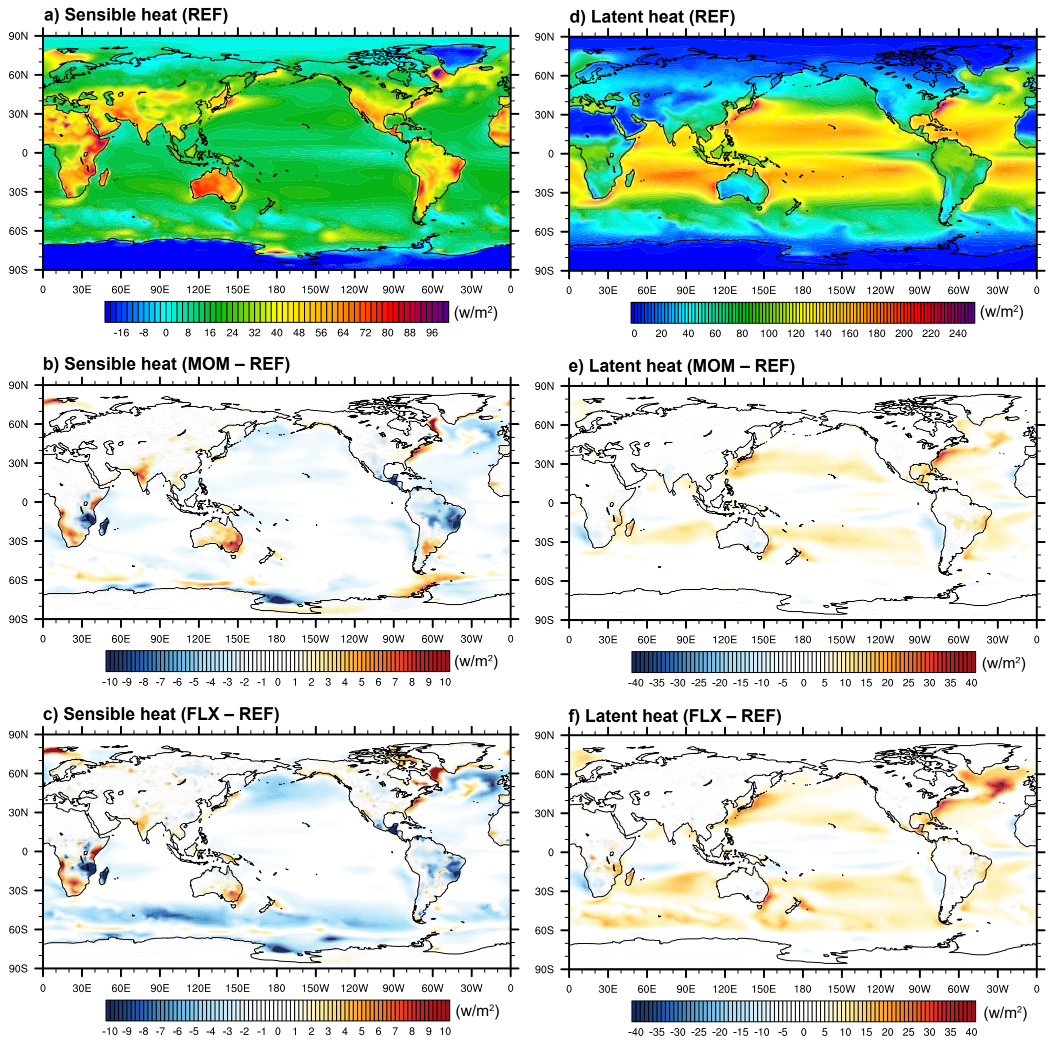

Figure 4. Total sensible (a,b,c) and latent (d,e,f) heat flux into the atmosphere in the simulations. All data are averaged in time from 1975 to 2014. (a) and (d) show the time mean sensible and latent heat flux for the REF simulation. (b) and (e) are the differences between MOM and REF simulations, (c) and (f) are the differences between FLX and REF.

cooling of the sea surface temperature in those regions. However, the latent heat flux change is more prominent than sensible heat flux. Unlike MOM, FLX transfers more latent heat into the Southern Ocean and North Atlantic atmosphere, in which region wave height is considerable.

4 Impact on Climate States

4.1 Atmospheric Circulation

Figure 5 compares the climatological mean zonal wind in our simulations with the ERA5 reanalysis (Hersbach et al., 2020) and among themselves. The REF simulation exhibits large bias at the latitudes of the barotropic jet, especially in the Southern Hemisphere and the stratosphere (Fig. 5a). The MOM simulation weakens midlatitude westerlies and tropical easterlies in the lower troposphere (Fig. 5d), thereby reducing the wind biases (Fig. 5b). Note that the upper-level subtropical jet

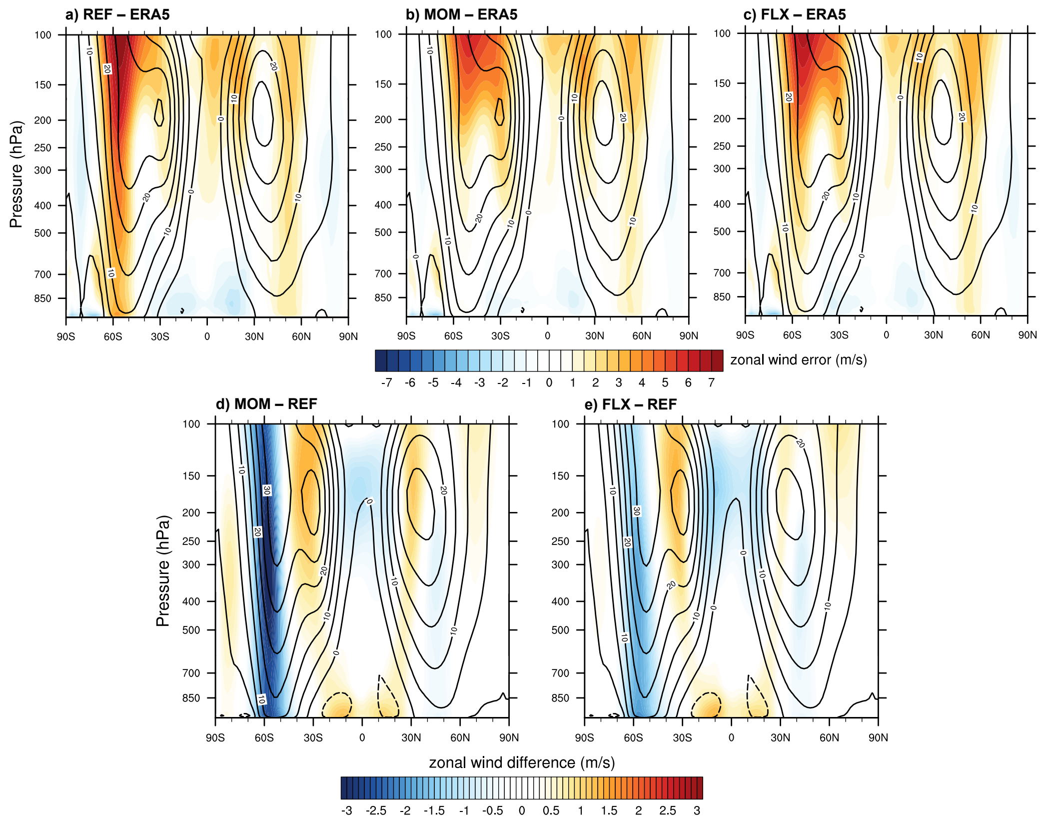

Figure 5. Time mean, zonal mean zonal wind in the simulations and observation. Contours in (a-c) are temporally and zonally averaged zonal wind in the ERA5 reanalysis, and color shading in (a-c) indicates differences between the CESM2 simulations and ERA5. Contours in (d) and (e) are temporally and zonally averaged zonal wind in the REF simulation, and color shading is the difference between MOM or FLX simulation and REF simulation. Negative values use dashed contours.

enhances as the midlatitude barotropic jet weakens (Fig. 5d); the change implies that baroclinic eddy activities, which transport momentum from the subtropical jets to barotropic jets, are suppressed in the MOM simulation due to the enhanced surface drag. The stratosphere jet bias shows little improvement, probably because the bias source is the relatively low model top in CESM2 and cannot be affected by lower-level changes. The FLX simulation exhibits reduced bias compared with the REF simulation, but it has a slightly larger bias than the MOM simulation in terms of the Southern Hemisphere barotropic jet (Fig. 5c and 5e). Given that the main difference between FLX and MOM simulations is the enhanced latent heat flux in the Southern Ocean and over the western boundary currents regions, the difference in zonal wind suggests the increased latent heat flux has the effect of enhancing baroclinic storms, which are the key to the strength of the barotropic jets.

The mean meridional circulation is shown in Fig. 6, in which the MOM and FLX show significant changes in the strength of the Hadley circulation. The weakening of the Hadley cells is consistent with the weakening of the lower-troposphere trade winds due to the new flux parameterization (Fig. 5), and it is probably caused by the weakened meridional winds as a result of the enhanced surface drag. The FLX simulation exhibits a more substantial decrease in the Hadley circulation's strength than the MOM simulation. This difference is intriguing because MOM and FLX share similar levels of enhanced surface drag (Fig. 2). A plausible explanation is that the

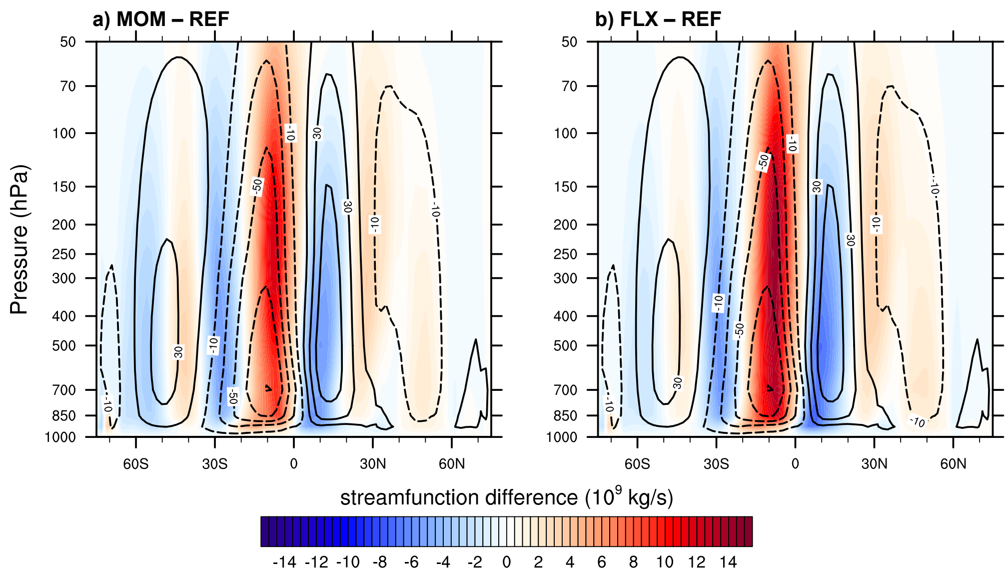

Figure 6. Meridional mass streamfunction of the atmospheric circulation. Contours are the streamfunction for the REF simulation, and negative values are indicated with dashed contours. Color shading is the difference between MOM or FLX simulation and REF simulation.

FLX simulation has more pronounced warming over continents compared with REF than the MOM simulation, which is detailed below in Fig. 9.

The last aspect of the general circulation we want to examine is the stationary wave patterns, which are critical in determining the zonal asymmetry of the climate (Kaspi & Schneider, 2011). Figure 7 shows the stationary wave component of the 700-hPa geopotential height field (Z^*) and the differences caused by the new parameterizations in MOM and FLX. The climatology of the stationary waves in the REF simulation exhibits anticyclonic circulation in the western part of continents and cyclonic circulation in the eastern side around the coasts in the Northern Hemisphere. Such patterns cause the extra-cold winters in Northeastern North America and Northeastern Asia. By introducing the wave-state-dependent flux parameterizations, the MOM and FLX simulations exhibit weakening of those stationary wave patterns in the extratropics of both the Northern and Southern Hemispheres. This weakening is likely due to the weakening of midlatitude barotropic westerly jets but can also be affected by the change in baroclinic eddies. The FLX simulation exhibits a more pronounced weakening of the positive Z^* anomalies in Europe and Western North America, which presumably result from the effects of enhanced latent heat flux on extratropical eddies.

4.2 Precipitation, Temperature, and Sea Ice

The effects of the new parameterization on global precipitation are most evident in the tropics and subtropical region (Fig. 8). Compared with the REF simulation, the MOM run exhibits decreased precipitation around the equator, with a larger reduction to the east of the maritime continent. On the other hand, the subtropical region exhibits increases in precipitation, especially in the eastern central Pacific and Indian Ocean and over the Amazon. These changes are consistent with the difference in the Hadley circulation we found above. The weakening of the Hadley circulation reduces rainfall in the deep tropics and allows more convection in the subtropics. The change in the eastern central Pacific and the Amazon suggests the Walker circulation also has a response to the changed surface momentum flux, probably a result of the Hadley circulation variation. Such responses of the subtropical rainfall associated with the Hadley circulation shift is further intensified in the FLX simulation. Rainfall is notably intensified over the Southern Indian Ocean, probably due

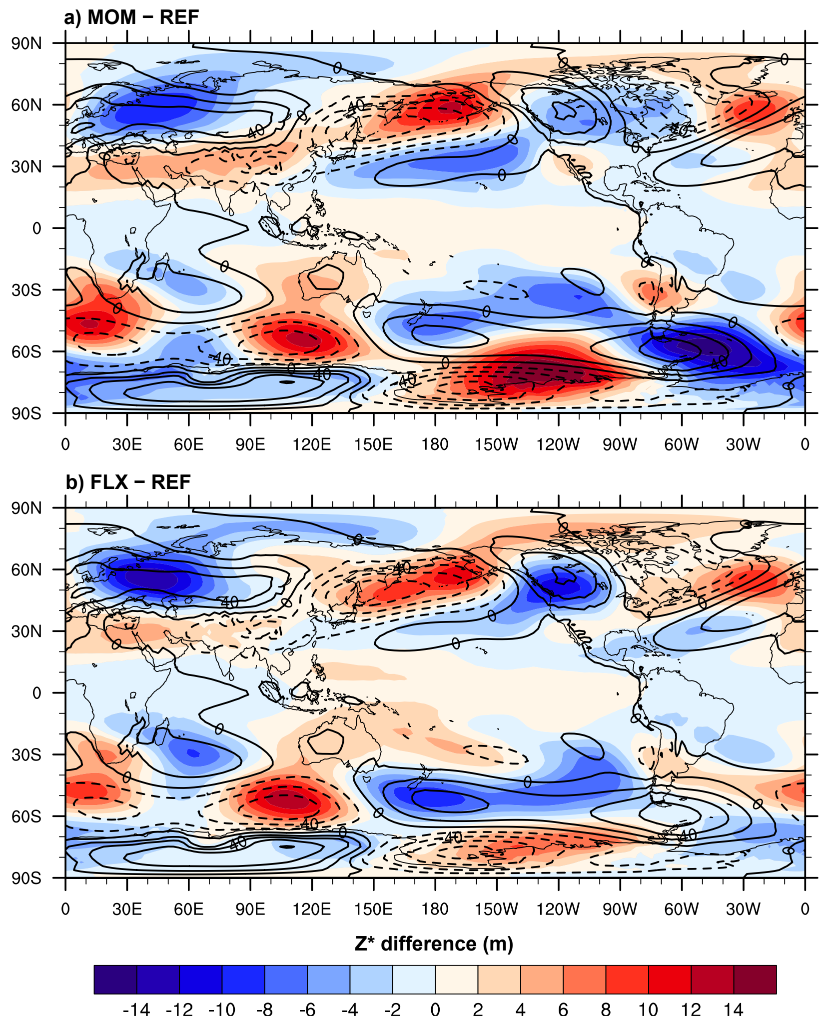

Figure 7. Stationary wave component of geopotential height (Z^*) at 700 hPa in the simulations. Z^* is the deviation of time mean geopotential height from the time and zonal mean values. Contours are the Z^* values of the REF simulation, and color shading is the difference between the MOM or FLX and REF simulations. Negative values are indicated with dashed contours.

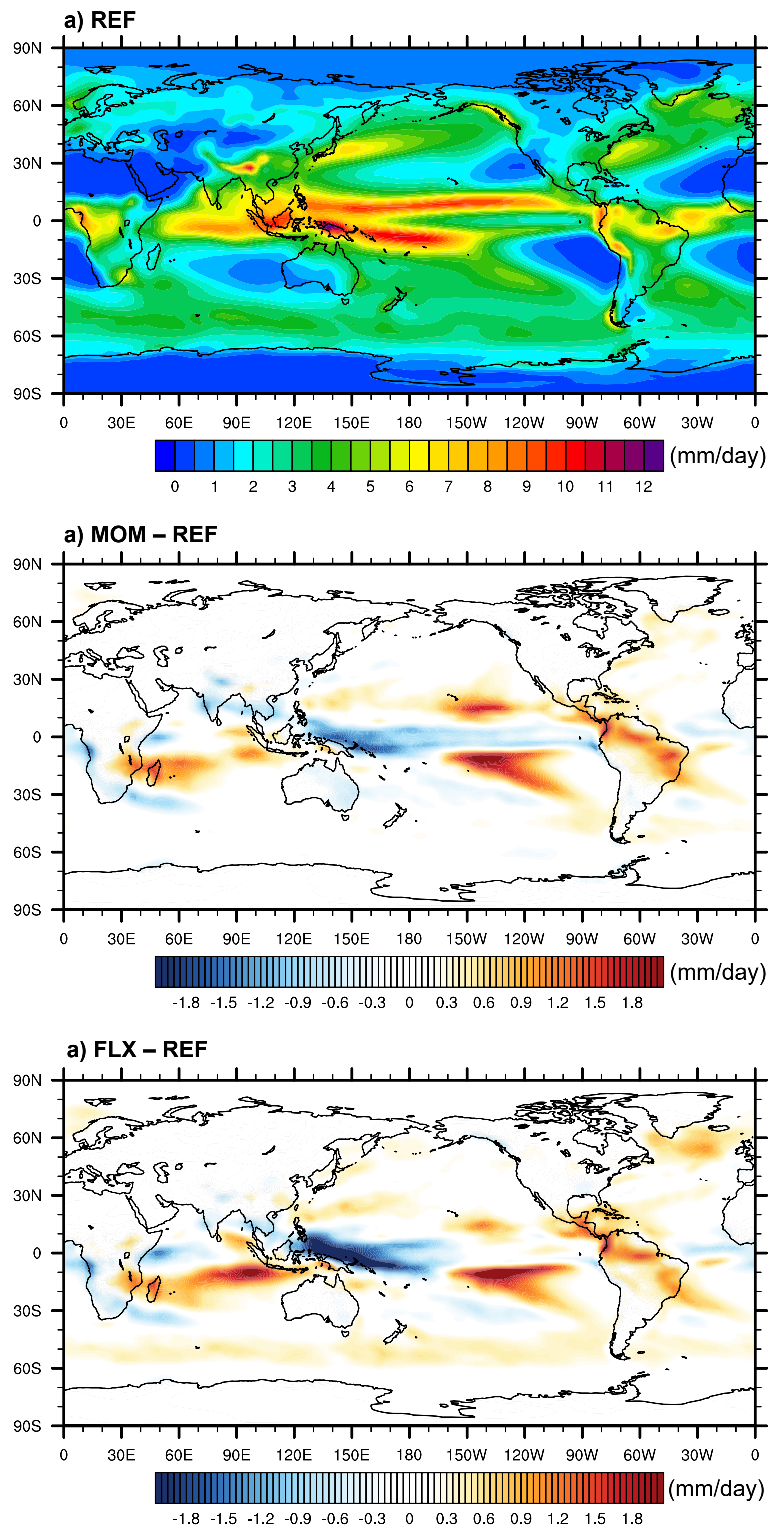

Figure 8. Time mean precipitation in the REF simulation (a), the difference in mean precipitation between MOM and REF simulations (b), and that between FLX and REF (c).

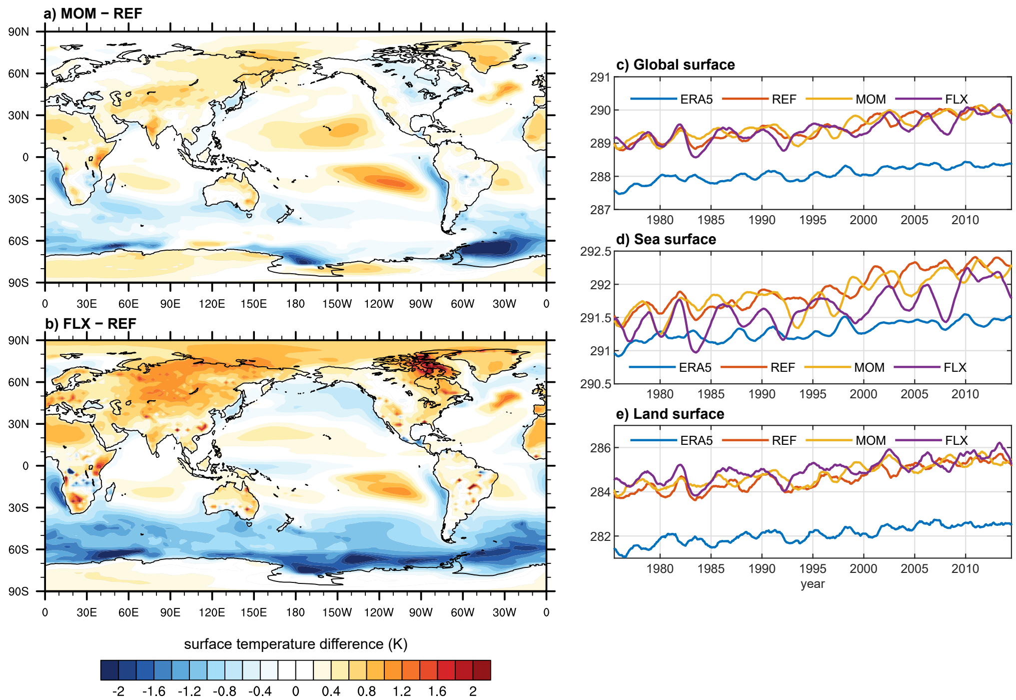

Figure 9. Time mean surface temperature difference between MOM and REF simulations (a) and that between FLX and REF simulations (b). (c-e) are the time series of the area mean surface temperature for (c) global average, (d) sea surface average, and (e) land surface average. Besides the three simulations, REF, MOM, and FLX, the time series for ERA5 surface temperature is also added for comparison. In (c), the time mean of ERA5, REF, MOM, and FLX are 288.07, 289.47, 289.48, and 289.39 K, respectively. In (d), they are 291.29, 291.91, 291.85, and 291.62 K, respectively. In (e), they are 282.09, 284.62, 284.81, and 285.01, respectively.

to the increase in surface latent flux to the south of it (Fig. 4), which enhances equatorward moisture transport.

Surface temperature change due to the new surface flux parameterization is shown in Fig. 9. In the MOM simulation, the temperature in the eastern subtropical Pacific Ocean exhibits warming compared with the REF simulation. This warming in the subtropics is likely in part a result of the change in the Hadley circulation, which caused increases in convection in those regions as suggested by the precipitation change (Fig. 8). When we compare the MOM and REF simulations, the longwave radiation at the model top has a consistent pattern (Fig. 10c,d) that exhibits warming anomalies over the eastern subtropical Pacific. Meanwhile, the poleward heat transport by the subtropical ocean gyres exhibits significant increases, which also contribute to the warming in subtropical ocean (c.f., Section 4.3). The temperature near the west coast of South America and Africa exhibits some cooling, probably due to the enhanced surface drag that strengthens upwelling near the coast. This cooling is additionally enhanced due to low-cloud feedback, which is evidenced by the model top radiation change (Fig. 10). Additionally, the change in surface drag might change the mixed layer depth through modulating the “wind work”, therefore impacting temperature in some regions (Luongo et al., 2024).

The FLX simulation exhibits a similar pattern of changes. However, the warming in the Northern Hemisphere subtropical Pacific becomes weaker and shifts westward. The cooling along the west coast of continents extends to North America as well. More pronounced differences between the MOM and FLX simulations include the enhanced warming over the northern Eurasia continent

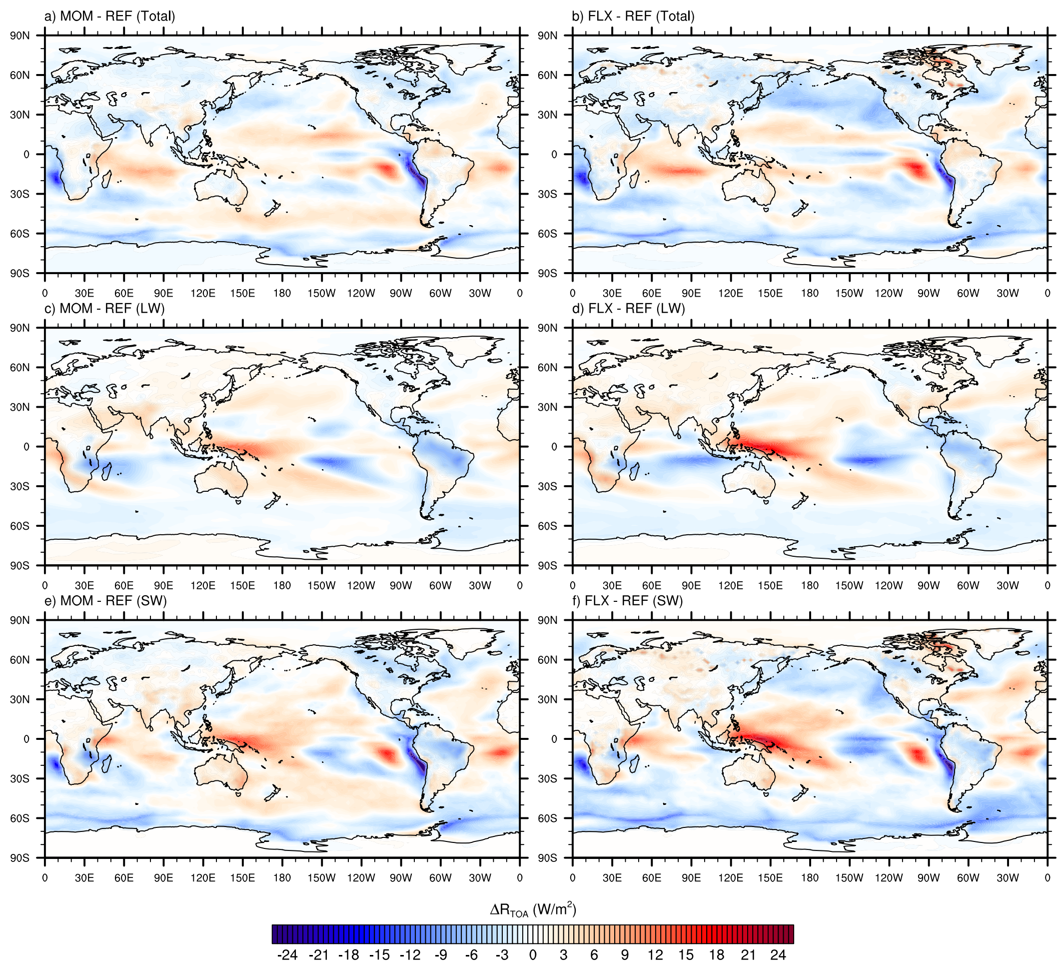

Figure 10. Time mean net radiation flux differences at the model top between MOM and REF (a,c,e) and between FLX and REF (b,d,f). (a) and (b) are net total radiative flux (shortwave + longwave); (c) and (d) are net longwave radiation; (e) and (f) are net shortwave radiation. The positive direction for total and shortwave is downward, and the positve direction for longwave is upward.

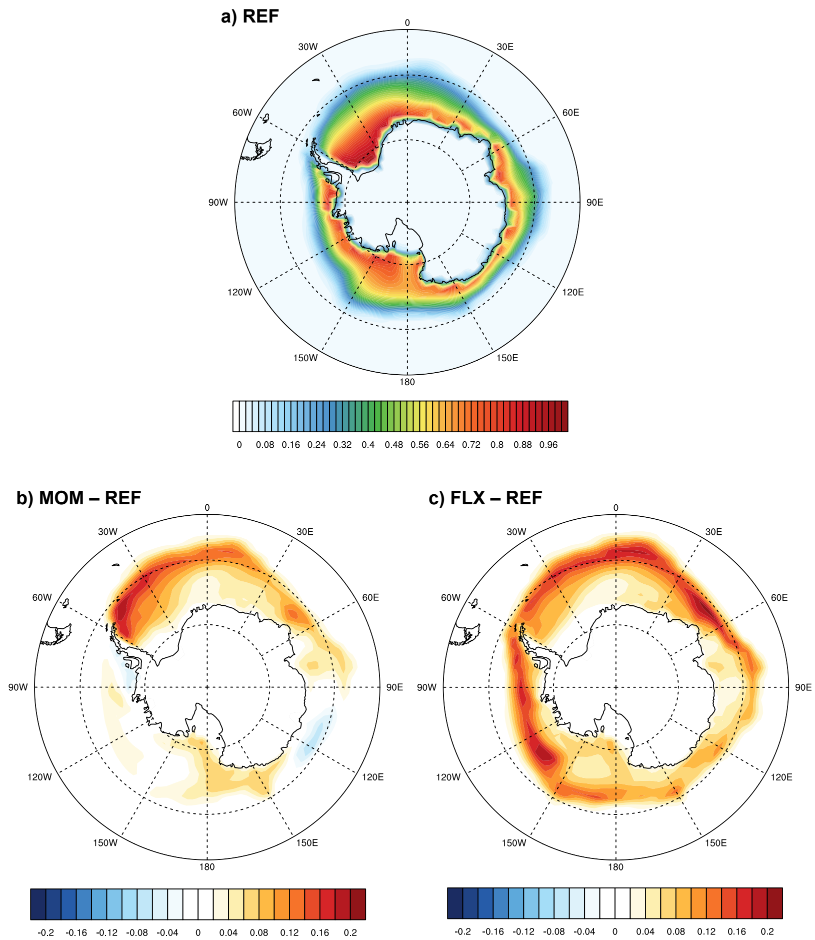

Figure 11. Time mean of the surface area fraction covered by sea ice in the simulations.

and the significant cooling in the Southern Ocean near the Antarctica coast. The warming over the Eurasia continent is likely a result of the change in stationary wave patterns, the weakening of which reduces the zonal asymmetry of midlatitude climate. North America's temperature also exhibits similar differences between MOM and FLX, though the magnitude of the difference is smaller. The strengthening of the Atlantic Meridional Overturning Circulation (AMOC) in FLX, discussed in the next section, may also contribute to the warming over the Eurasia continent in FLX. The cooling in the Southern Ocean happens in tandem with seasonal sea ice changes, which are discussed below when we document the sea ice responses.

Figure 9c–d shows the global mean, global sea-surface mean, and global land-surface mean temperature in the 40 years of the simulations. The time series of ERA5 reanalysis surface temperature is also included for comparison. The model simulations show a warm bias of 1.3 K regarding the global mean. Global land-surface mean temperature is 0.2 and 0.4 K higher than in the REF run in the MOM and FLX simulations, respectively. In contrast, the global ocean surface temperature exhibits pronounced differences between the FLX simulation and others. On average, the FLX simulation has a cooler ocean surface (0.3 K colder than REF), closer to the ERA5 sea surface temperature. However, the oceans' inter-decadal variability in the FLX simulation seems excessively large compared with that in ERA5 data.

Another interesting finding about the new surface flux schemes is that sea ice near the Antarctic coast is very sensitive to changes in surface stress and fluxes. Figure 11a shows the climatological mean sea ice area fraction in the Antarctic region, and Figure 11b and 11c are the changes due to introducing the new wave-state dependent surface flux parameterizations. In MOM, where wind stress is modified, time mean ice fraction increases in the Weddle Sea. It has been suggested that wind-driven ice advection is an essential mechanism in governing the ice concentration around West Antarctica, and strengthened westerly is responsible for sea ice loss in some years (Holland & Kwok, 2012; Turner et al., 2020). Thus, the increase in sea ice in the Weddle Sea in our MOM simulations directly results from the enhanced drag coefficient and the weakened westerlies in the lower troposphere.

In contrast, the FLX simulation exhibits increased sea ice cover around Antarctica for all longitudes. The difference between the FLX and MOM simulation is the decreased sensible heat and increased latent heat flux. The former can directly reduce near-surface air temperature. The latter can enhance clouds, especially those at low levels. We evaluated the net radiative flux at the model top (Fig. 10) and found that FLX exhibits decreases in the shortwave flux at mid- and high-latitudes in the Southern Hemisphere, whereas the MOM simulation does not share similar decreases in shortwave flux.

It should be noted that once sea ice forms and expands northward, it can cut off sensible flux from the relatively warm water, thereby further lowering near-surface air temperature and enhancing sea ice expansion. Therefore, the increases of sea ice in FLX compared with MOM and REF likely involve the interaction between surface flux, cloud, and sea ice. The temperature decrease pattern (Fig. 9) around the Antarctica does not resemble the pattern of sensible or latent heat flux changes (Fig. 4). Thus, the increases in sea ice appear to play a more direct role in the substantial decreases in the sea surface temperature in the Southern Ocean, which yield favorable improvement to reduce the ocean surface temperature bias in the simulations. The Arctic region does not share similar increases due to the new surface flux parameterization. Actually, it exhibits slight decreases ($< 5\%$) in the sea ice fraction in the Asian-side Arctic region, probably due to the corresponding temperature change.

4.3 Ocean Meridional Overturning Circulation

The global meridional overturning circulation (MOC) in the simulations is shown in Fig. 12. The dominant features are the Atlantic Meridional Overturning Circulation (AMOC) and the Southern Meridional Overturning Circulation (SMOC). Introducing the wave-dependent wind stress in the MOM simulation does not affect the AMOC much. However, the SMOC's subsiding branch related to the Antarctic Intermediate Water is enhanced, and its upwelling branch related to the Circumpolar Deep Water is weakened. This northward shift of SMOC may be primarily due to the wind stress change but could be affected to some extent by the sea ice change.

In contrast, the FLX simulation significantly strengthens the subsiding branch of the AMOC. Figure 4 shows that near the surface, latent heat flux is substantially enhanced to the south of Greenland, where wave height is large due to wave dynamics (Fig. 3). The response in AMOC is likely due to the cooling and the increase in salinity of the near-surface water in the North Atlantic as the latent heat flux is enhanced in FLX.

The meridional heat transport by the ocean circulation is shown in Fig. 12e. The largest changes in amplitudes are in subtropical regions. MOM and FLX exhibit increasingly stronger poleward heat transport peaking around 15°N/S. Their peaks are about 20% higher than that in the REF simulation. The heat transport at those latitudes is generated by the shallow overturning circulations associated with subtropical gyres, which are driven by atmospheric winds. Approximately between 40° and 50° in the Southern and Northern Hemispheres, the differences between MOM and REF is small, but their poleward heat fluxes are weaker than that of the FLX simulation by about 10%. Those differences are due to changes in the deeper thermohaline circulations. The enhancement of AMOC probably contributed to the Eurasia continent warming in FLX compared with MOM and REF. The changes in meridional heat transport is mainly caused by changes in the Eulerian mean circulation in the ocean, eddies' contribution is minimal.

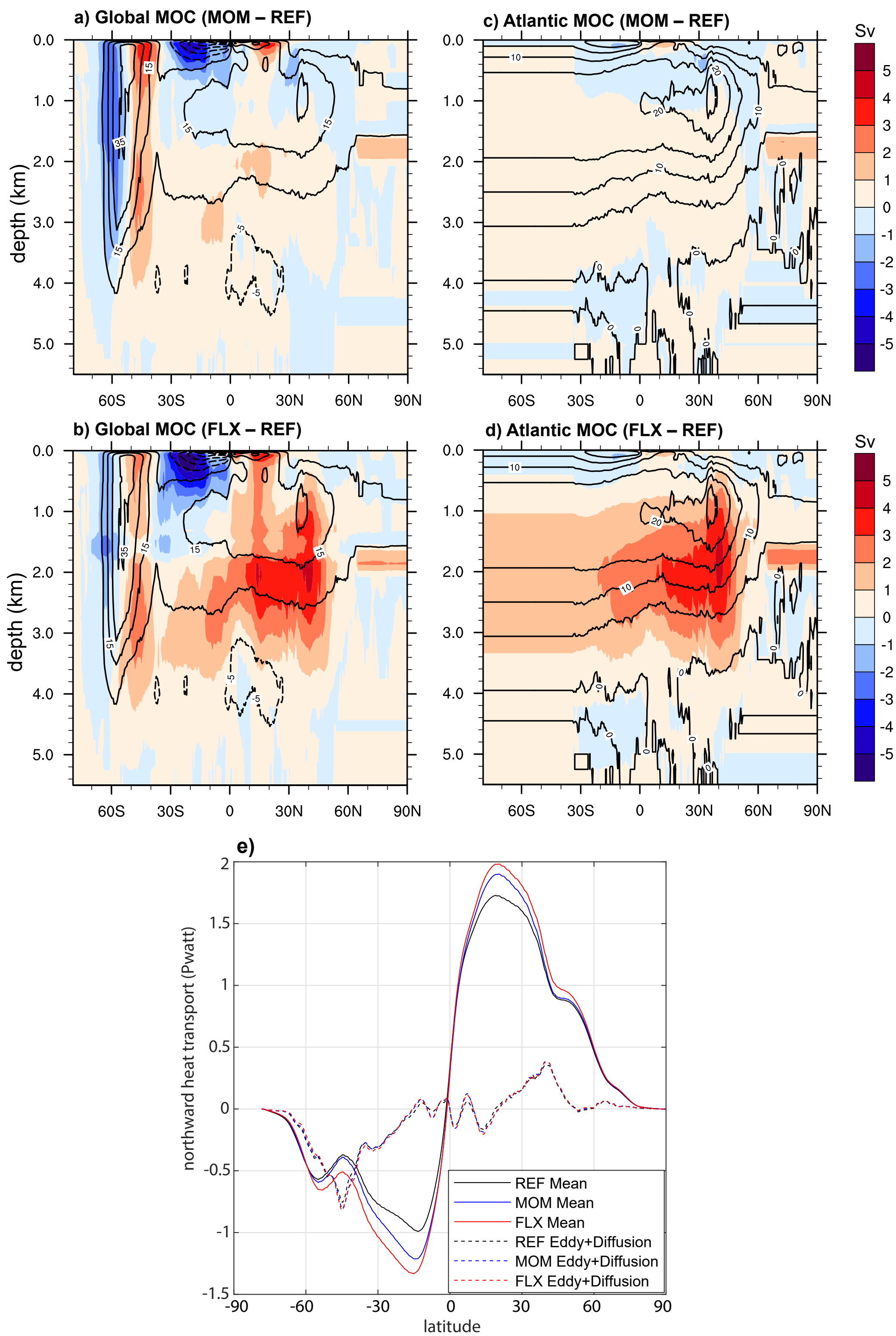

Figure 12. Ocean meridional overturning circulation (MOC) for the globe (a,b) and Atlantic (c,d) and the global meridional heat transport by the ocean (e). In (a-d), Contours show the streamfunction of the REF simulation, and color shading is the difference between MOM or FLX simulations and the REF simulation. In (e), solid lines show the time mean total meridional heat flux of different simulations, and dashed lines show the contribution from eddies and diffusion.

4.4 Natural and Forced Variability

Lastly, we evaluate how the new surface flux schemes impact natural variability and anthropogenic temperature change. The Oceanic Niño Index time series in our three simulations and the ERA reanalysis are shown in Figure 13. Compared with the ERA5 reanalysis (Fig. 13d), the ENSO in the REF simulation has relatively large amplitudes. The MOM and FLX simulations inherit that and exhibit an even slightly larger amplitude bias. However, a notable improvement is the frequency of ENSO in the simulations. The REF simulation's ENSO has a more regular frequency of about two years. The FLX simulation's ENSO has more variation in the frequency, and it maintains a positive phase for five years from 1993 to 1998. This extended period is more consistent with the ERA5 reanalysis, which maintained a positive phase from 1991 to 1996. The MOM simulation also has a similar but less impressive improvement. While we acknowledge that these simulations are too short to fairly assess the model's performance in simulating ENSO, it is interesting to see the sensitivity of simulated ENSO frequency to the wave-state dependent air-sea fluxes here.

Figure14 shows the surface temperature change from the first ten-year period (1975-1984) to the last ten-year period (2005-2014) in our simulations and the ERA5 reanalysis. A notable bias of climate change in the REF simulation is the warming in northern Asia, which is too strong compared with the reanalysis. MOM and FLX simulations reduced the warming bias in the northern Asia continent.

Another substantial improvement is in the eastern Pacific region, where coupled climate models in CMIP6 persistently exhibit warming in recent decades while observation indicates slight cooling (Seager et al., 2022; Wills et al., 2022). The MOM simulation can reproduce the cooling over the recent decades in the Southern Hemisphere, eastern tropical and subtropical Pacific, but still has a warming bias in the Northern Hemisphere Pacific near the west coast of North America.

Interestingly, the FLX simulation can reproduce the rough cooling pattern in the eastern Pacific in both hemispheres. However, the cooling in the Southern Ocean is still too weak in FLX, and off the coast of northern Japan, FLX suffers from a warming bias. Those issues might be related to the coarse resolutions of all components in our simulations, especially the WW3 module. However, it should be noted that the Extended Reconstructed SST data set v5 (ERSSTv5) (Huang et al., 2017) indeed exhibits some relatively strong warming trend to the east of Japan, which is mild in ERA5 reanalysis (Wills et al., 2022).

5 Summary and Discussion

By analyzing the wind biases in climate simulations compared with reanalysis, Simpson et al. (2018) suggest that there might be a missing process in climate models that constitutes a missing drag on the low-level zonal flow over oceans. Conventional air-sea flux parameterizations estimate fluxes from near-surface atmospheric stability and air-sea differences in velocity, temperature, and water vapor. However, the presence of ocean surface gravity waves introduces additional variability that cannot be described by atmospheric stability or air-sea differences. In this study, we implemented a wave-state-dependent surface flux parameterization in CESM2 and evaluated its impact on the mean climate states and historical trends. Surface momentum flux is modified through wave-dependent roughness lengths, and sensible and latent heat fluxes are modified through the new roughness formula and considering the effects of sea spray. The surface drag coefficient for momentum increases at all latitudes in the simulations with the new parameterization, but surface wind stress shows decreases at some latitudes, such as over the Southern Ocean and the central Pacific near the equator. Those changes in surface wind stress, on the one hand, depend on the regional characteristics of waves and, on the other hand, depend on the mean state change in the atmospheric circulation. Sea-spray dependency, in general, decreases surface sensible heat flux and increases latent heat flux. The latter dominates and exhibits significant changes in mid- and high-latitude oceans.

The new wave-dependent schemes bring noticeable changes in the mean climate states into the simulations in CESM2. High bias in the Southern Hemisphere barotropic jet is reduced, especially in the lower and middle troposphere. Hadley Circulation is weakened due to the new schemes, causing

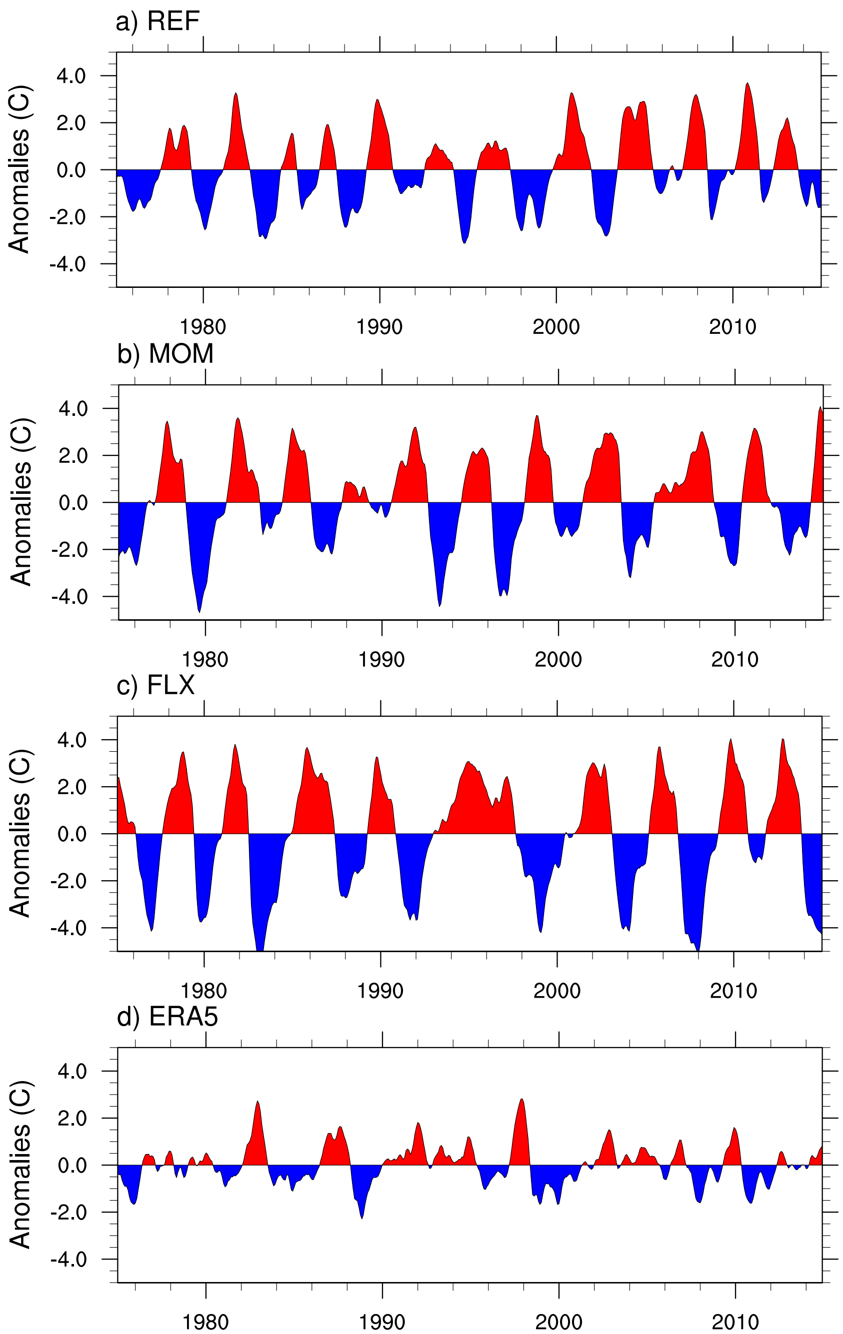

Figure 13. Time series of Oceanic Niño Index (ONI) in the simulations (a-c) and ERA5 reanalysis. The ONI is defined as the 3-month running means of sea surface temperature anomalies in the Niño 3.4 region (5°N-5°S, 120°–170°W).

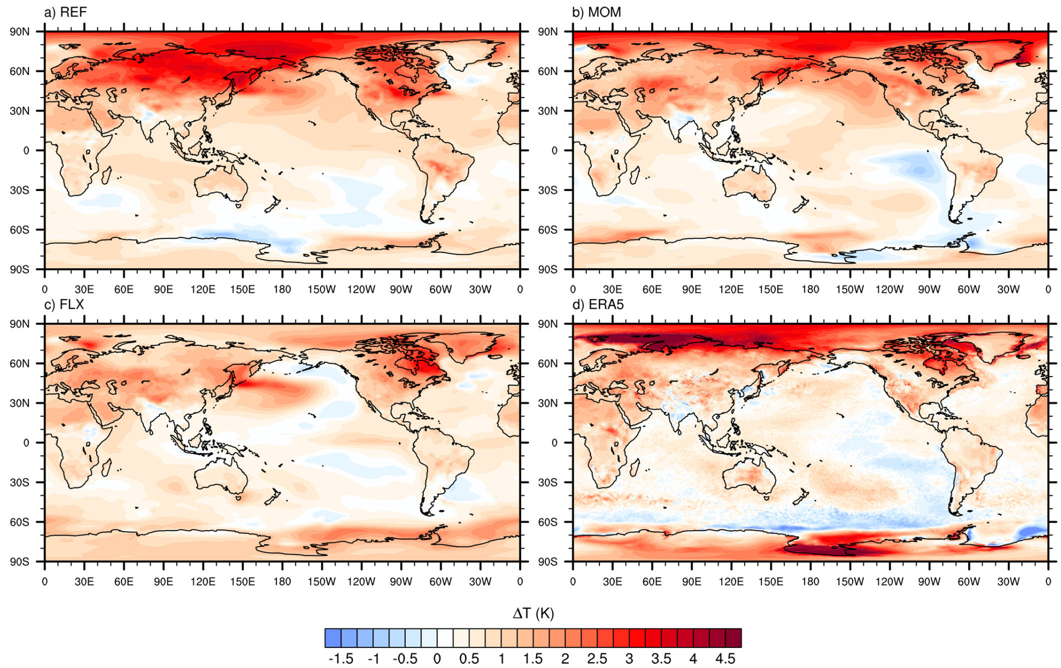

Figure 14. Temperature difference between the time average of the last ten years (2005–2014) and first ten years (1975-1984) of the three simulations and the ERA5 reanalysis.

decreases in the precipitation in the deep tropics to the east of the maritime continents and increases in the eastern subtropical Pacific. Extratropical stationary wave patterns are weakened, leading to a more zonally symmetric climate. Notable differences in surface temperature are exhibited with those circulation changes, especially in the FLX simulation, which includes both the new momentum and enthalpy flux schemes. Compared with the reference simulation without those new schemes, the FLX simulation exhibits warmer temperatures over the northern Asia continent and a significantly cooler Southern Ocean. The temperature change in the Southern Ocean is related to the expansion of sea ice around Antarctica, which is likely a result of the effects of enhanced surface latent heat flux on low clouds.

The new surface flux schemes also have an important impact on the ocean. The slight cooling in the eastern Pacific in recent decades is missing in the reference run, but it is reproduced in the FLX simulation with both the new momentum and enthalpy flux parameterizations. The new schemes also substantially enhance the mean strength of the Atlantic Meridional Overturning Circulation, likely through increasing the salinity of upper-level water in the North Atlantic by enhancing evaporation.

Our simulations still have notable biases in various metrics, such as the global mean land surface temperature. Those biases might be due to the coarse resolutions we used in the atmosphere and wave components of the CESM2 simulations. The low resolution might under-resolve details of atmospheric and ocean dynamics, and more importantly, parameterization schemes are likely tuned for the default CESM2 resolutions. Therefore, they probably produce biases when the model is run at the coarse resolutions. Additionally, even at standard resolutions, adding a new parameterization to some extent requires tuning other parameterizations in CESM2, which we did not do. Our simulations are also relatively short and, therefore, likely contaminated by low-frequency variability. While we seek a physically reasonable understanding of the impact of the new surface flux parameterizations, the complex feedback in a fully coupled Earth system model means that the improvements and remaining biases might result from coupled dynamics instead of being caused by a single process. Nevertheless, our experiments demonstrate that including wave-state dependency in surface flux parameterizations has excellent potential to elevate the fidelity of Earth system simulations. More investigation with refined resolutions and carefully tuned parameters is warranted in future studies.

Open Research Section

The official version of the CESM2 code is publicly available at https://github.com/ESCOMP/CESM. The modified code with wave-dependent surface flux parameterizations involves several modules of CESM2 are deposited at https://github.com/MetLab-HKUST/Flux-CIME, https://github.com/MetLab-HKUST/Flux-WW3, and https://github.com/MetLab-HKUST/Flux-CAM. The ERA5 reanalysis is publicly available at the Climate Data Store (https://cds.climate.copernicus.eu/).

Acknowledgments

The work described in this paper was substantially supported by a grant from the Research Grants Council of the Hong Kong Special Administrative Region, China (Project Reference Number: AoE/P-601/23-N). XS and QL are also supported by the Center for Ocean Research in Hong Kong and Macau (CORE), a joint research center between the Laoshan Laboratory and the Hong Kong University of Science and Technology (HKUST). The authors thank HKUST Fok Ying Tung Research Institute and the National Supercomputing Center in Guangzhou Nansha sub-center for providing high-performance computational resources.

References

Andreas, E. L. (1989). Thermal and size evolution of sea spray droplets. crrel report 89-11. *US Army Cold Regions Research and Engineering Laboratory, Hanover, NH (NTIS ADA210484)*.

Andreas, E. L. (1990). Time constants for the evolution of sea spray droplets. *Tellus B*, *42*(5), 481–497.

Andreas, E. L. (1992). Sea spray and the turbulent air-sea heat fluxes. *Journal of Geophysical Research: Oceans*, *97*(C7), 11429–11441.

Andreas, E. L. (1995). The temperature of evaporating sea spray droplets. *Journal of Atmospheric Sciences*, *52*(7), 852–862.

Andreas, E. L. (1998). A new sea spray generation function for wind speeds up to 32 ms- 1. *Journal of Physical Oceanography*, *28*(11), 2175–2184.

Andreas, E. L., Mahrt, L., & Vickers, D. (2015). An improved bulk air–sea surface flux algorithm, including spray-mediated transfer. *Quarterly Journal of the Royal Meteorological Society*, *141*(687), 642–654.

Andreas, E. L., Persson, P. O. G., & Hare, J. E. (2008). A bulk turbulent air–sea flux algorithm for high-wind, spray conditions. *Journal of Physical Oceanography*, *38*(7), 1581–1596.

Bao, Y., Song, Z., & Qiao, F. (2020). Fio-esm version 2.0: Model description and evaluation. *Journal of Geophysical Research: Oceans*, *125*(6), e2019JC016036.

Barsugli, J. J., & Battisti, D. S. (1998). The basic effects of atmosphere–ocean thermal coupling on midlatitude variability. *Journal of the Atmospheric Sciences*, *55*(4), 477–493.

Bernardet, L., Tallapragada, V., Bao, S., Trahan, S., Kwon, Y., Liu, Q., . . . others (2015). Community support and transition of research to operations for the hurricane weather research and forecasting model. *Bulletin of the American Meteorological Society*, *96*(6), 953–960.

Cavaleri, L., Fox-Kemper, B., & Hemer, M. (2012). Wind waves in the coupled climate system. *Bulletin of the American Meteorological Society*, *93*(11), 1651–1661.

Chen, G., Chapron, B., Ezraty, R., & Vandemark, D. (2002). A global view of swell and wind sea climate in the ocean by satellite altimeter and scatterometer. *Journal of Atmospheric and Oceanic Technology*, *19*(11), 1849–1859.

Chen, S. S., Zhao, W., Donelan, M. A., & Tolman, H. L. (2013). Directional wind–wave coupling in fully coupled atmosphere–wave–ocean models: Results from cblast-hurricane. *Journal of the Atmospheric Sciences*, *70*(10), 3198–3215.

Emanuel, K. A. (1986). An air-sea interaction theory for tropical cyclones. Part I: Steady-state maintenance. *Journal of Atmospheric Sciences*, *43*(6), 585–605.

Fairall, C. W., Bradley, E. F., Hare, J., Grachev, A. A., & Edson, J. B. (2003). Bulk parameterization of air–sea fluxes: Updates and verification for the coare algorithm. *Journal of climate*, *16*(4), 571–591.

Fischer, E., Beyerle, U., Schleussner, C.-F., King, A. D., & Knutti, R. (2018). Biased estimates of changes in climate extremes from prescribed sst simulations. *Geophysical Research Letters*, *45*(16), 8500–8509.

He, J., & Soden, B. J. (2016). Does the lack of coupling in sst-forced atmosphere-only models limit their usefulness for climate change studies? *Journal of Climate*, *29*(12), 4317–4325.

Hersbach, H., Bell, B., Berrisford, P., Hirahara, S., Horányi, A., Muñoz-Sabater, J., . . . others (2020). The era5 global reanalysis. *Quarterly Journal of the Royal Meteorological Society*, *146*(730), 1999–2049.

Hirons, L., Klingaman, N., & Woolnough, S. (2018). The impact of air-sea interactions on the representation of tropical precipitation extremes. *Journal of Advances in Modeling Earth Systems*, *10*(2), 550–559.

Holland, P. R., & Kwok, R. (2012). Wind-driven trends in antarctic sea-ice drift. *Nature Geoscience*, *5*(12), 872–875.

Huang, B., Thorne, P. W., Banzon, V. F., Boyer, T., Chepurin, G., Lawrimore, J. H., . . . Zhang, H.-M. (2017). Extended reconstructed sea surface temperature, version 5 (ersstv5): upgrades, validations, and intercomparisons. *Journal of Climate*, *30*(20), 8179–8205.

Kaspi, Y., & Schneider, T. (2011). Winter cold of eastern continental boundaries induced by warm ocean waters. *Nature*, *471*(7340), 621–624.

Lee, J., Planton, Y. Y., Gleckler, P. J., Sperber, K. R., Guilyardi, E., Wittenberg, A. T., . . . Pallotta, G. (2021). Robust evaluation of enso in climate models: How many ensemble members are needed? *Geophysical Research Letters*, *48*(20), e2021GL095041.

Lin, S., & Sheng, J. (2020). Revisiting dependences of the drag coefficient at the sea surface on wind speed and sea state. *Continental Shelf Research*, *207*, 104188.

Lin, S., Sheng, J., Ohashi, K., & Song, Q. (2021). Wave-current interactions during hurricanes earl and igor in the northwest atlantic. *Journal of Geophysical Research: Oceans*, *126*(12), e2021JC017609.

Liu, J., Curry, J. A., Clayson, C. A., & Bourassa, M. A. (2011). High-resolution satellite surface latent heat fluxes in north atlantic hurricanes. *Monthly Weather Review*, *139*(9), 2735–2747.

Luongo, M. T., Brizuela, N. G., Eisenman, I., & Xie, S.-P. (2024). Retaining short-term variability reduces mean state biases in wind stress overriding simulations. *Journal of Advances in Modeling Earth Systems*, *16*(2), e2023MS003665.

Mogensen, K. S., Magnusson, L., & Bidlot, J.-R. (2017). Tropical cyclone sensitivity to ocean coupling in the e cmwf coupled model. *Journal of Geophysical Research: Oceans*, *122*(5), 4392–4412.

Neale, R. B., Chen, C.-C., Gettelman, A., Lauritzen, P. H., Park, S., Williamson, D. L., . . . others (2010). Description of the NCAR community atmosphere model (CAM 5.0). *NCAR Tech. Note NCAR/TN-486+ STR*, *1*(1), 1–12.

Newman, M., Sardeshmukh, P. D., & Penland, C. (2009). How important is air–sea coupling in enso and mjo evolution? *Journal of Climate*, *22*(11), 2958–2977.

Olabarrieta, M., Warner, J. C., Armstrong, B., Zambon, J. B., & He, R. (2012). Ocean-atmosphere dynamics during hurricane ida and nor'ida: An application of the coupled ocean-atmosphere-wave-sediment transport (coawst) modeling system. *Ocean Modelling*, *43*, 112–137.

Pianezze, J., Barthe, C., Bielli, S., Tulet, P., Jullien, S., Cambon, G., . . . Cordier, E. (2018). A new coupled ocean-waves-atmosphere model designed for tropical storm studies: Example of tropical cyclone bejisa (2013–2014) in the south-west indian ocean. *Journal of Advances in Modeling Earth Systems*, *10*(3), 801–825.

Qiao, F., Song, Z., Bao, Y., Song, Y., Shu, Q., Huang, C., & Zhao, W. (2013). Development and evaluation of an earth system model with surface gravity waves. *Journal of Geophysical Research: Oceans*, *118*(9), 4514–4524.

Seager, R., Henderson, N., & Cane, M. (2022). Persistent discrepancies between observed and modeled trends in the tropical pacific ocean. *Journal of Climate*, *35*(14), 4571–4584.

Semedo, A., Sušelj, K., Rutgersson, A., & Sterl, A. (2011). A global view on the wind sea and swell climate and variability from era-40. *Journal of Climate*, *24*(5), 1461–1479.

Shimura, T., Mori, N., Takemi, T., & Mizuta, R. (2017). Long-term impacts of ocean wave-dependent roughness on global climate systems. *Journal of Geophysical Research: Oceans*, *122*(3), 1995–2011.

Simpson, I. R., Bacmeister, J. T., Sandu, I., & Rodwell, M. J. (2018). Why do modeled and observed surface wind stress climatologies differ in the trade wind regions? *Journal of Climate*, *31*(2), 491–513.

Song, Z., Qiao, F., & Song, Y. (2012). Response of the equatorial basin-wide sst to non-breaking surface wave-induced mixing in a climate model: An amendment to tropical bias. *Journal of Geophysical Research: Oceans*, *117*(C11).

Turner, J., Guarino, M. V., Arnatt, J., Jena, B., Marshall, G. J., Phillips, T., . . . others (2020). Recent decrease of summer sea ice in the weddell sea, antarctica. *Geophysical Research Letters*, *47*(11), e2020GL087127.

Wada, A., Kanada, S., & Yamada, H. (2018). Effect of air-sea environmental conditions and interfacial processes on extremely intense typhoon haiyan (2013). *Journal of Geophysical Research: Atmospheres*, *123*(18), 10–379.

Warner, J. C., Armstrong, B., He, R., & Zambon, J. B. (2010). Development of a coupled ocean–atmosphere–wave–sediment transport (coawst) modeling system. *Ocean modelling*, *35*(3), 230–244.

Wills, R. C., Dong, Y., Proistosecu, C., Armour, K. C., & Battisti, D. S. (2022). Systematic climate model biases in the large-scale patterns of recent sea-surface temperature and sea-level pressure change. *Geophysical Research Letters*, *49*(17), e2022GL100011.

Yu, H., Chen, P., Li, Q., & Tang, B. (2013). Current capability of operational numerical models in predicting tropical cyclone intensity in the western north pacific. *Weather and forecasting*, *28*(2), 353–367.

Zhao, B., Wang, G., Zhang, J. A., Liu, L., Liu, J., Xu, J., . . . others (2022). The effects of ocean surface waves on tropical cyclone intensity: Numerical simulations using a regional atmosphere-ocean-wave coupled model. *Journal of Geophysical Research: Oceans*, *127*(11), e2022JC019015.

Zhu, J., & Shukla, J. (2013). The role of air–sea coupling in seasonal prediction of asia–pacific summer monsoon rainfall. *Journal of Climate*, *26*(15), 5689–5697.